How does riming influence the observed spatial variability of ice water in mixed-phase clouds?

Nina Maherndl[1], Manuel Moser[2,3], Imke Schirmacher[4], Aaron Bansemer[6], Johannes Lucke[3,5], Christiane Voigt[2,3], and Maximilian Maahn[1]

[1]Leipzig Institute of Meteorology (LIM), Leipzig University, Leipzig, Germany
[2]Institute for Physics of the Atmosphere, Johannes Gutenberg University, Mainz, Germany
[3]Institute for Physics of the Atmosphere, German Aerospace Center (DLR), Wessling, Germany
[4]Institute for Geophysics and Meteorology, University of Cologne, Cologne, Germany
[5]Faculty of Aerospace Engineering, Delft University of Technology, Delft 2629, the Netherlands
[6]NSF National Center for Atmospheric Research, Boulder, Colorado, USA

Correspondence: Nina Maherndl (nina.maherndl@uni-leipzig.de)

Abstract.

Mixed-phase clouds (MPC) are a key component of the Earth's climate system. Observations show that ice water content (IWC) is not distributed homogeneously in MPC. Instead, high IWC tends to occur in clusters. However, it is not sufficiently understood which ice crystal formation and growth processes play a dominant role in IWC clustering in clouds. One important ice growth process is riming, which occurs when liquid water droplets freeze onto ice crystals upon contact. Here, airborne measurements of MPC in mid- and high-latitudes are used to study spatial variability of ice clusters in clouds and investigate how this variability is linked to riming. We use data from the IMPACTS (mid-latitudes) and the HALO-(AC)³ (high-latitudes) aircraft campaigns, where spatially and temporally collocated cloud radar and in situ measurements were collected. We derive riming and IWC by combining cloud radar and in situ measurements. Ice cluster scales and IWC variability in clouds are quantified using pair correlation functions. By comparing IWC calculations accounting for riming to IWC calculations neglecting riming, we single out the influence of riming.

During all analyzed flight segments, riming is responsible for 66 % and 63 % of total IWC during IMPACTS and HALO-(AC)³, respectively. In mid-latitude MPC, riming does not significantly change IWC cluster scales, but increases the probability of clusters occurrence. This enhancement occurs at similar scales as liquid water content variability. In cold air outbreak MPC observed during HALO-(AC)³, riming impacts IWC clustering at two distinctive scales. First, riming enhances the probability of in-cloud IWC clusters at spatial scales below 2 km, which corresponds to the wavelength of the roll cloud updraft and circulation features. Second, riming leads to additional in-cloud IWC clustering at spatial scales of 3-5 km. We find that the presence of mesoscale updraft features leads to enhanced occurrences of riming and therefore additional IWC clustering. An increased liquid water path might increase the effect, but is not a necessary criterion. These results help to improve our understanding of how riming is linked to IWC variability in clouds and can be used to evaluate and constrain models of MPC.

1 Introduction

In mid- and high-latitudes, most precipitation stems from ice containing clouds (Mülmenstädt et al., 2015), which are a crucial component of the Earth's weather and climate systems. In mixed-phase clouds (MPC), ice particles and supercooled liquid droplets coexist down to temperatures of about -38 °C in a thermodynamically unstable state. Mass and the ratio of ice and liquid particles play a critical role not only in precipitation processes, but also cloud lifetime, radiative budget (Sun and Shine, 1994; Shupe and Intrieri, 2004; Turner, 2005), and climate feedbacks (Choi et al., 2014; Bjordal et al., 2020).

Numerical forecast and climate models often fail to realistically predict or reproduce MPC properties, lifetime and precipitation amounts (Morrison et al., 2012, 2020; Ong et al., 2024; Connelly and Colle, 2019). The misrepresentation of MPC and ice clouds has been suggested as large contributor to the uncertainty in CMIP6 climate model predictions (e.g., Bock et al., 2021). This is in part linked to a poor understanding of ice formation and growth processes in MPC (Korolev et al., 2017). Their representations are therefore likely incomplete, even in sophisticated cloud microphysics schemes (e.g., Cao et al., 2023), such as the predicted particle properties (P3) scheme proposed by Morrison and Milbrandt (2015). Gaps in our understanding of dominating ice processes hamper progression in representing MPC in models (Morrison et al., 2012).

One important ice growth process is riming, which describes the process of supercooled droplets freezing onto ice particles after contact. Riming efficiently converts liquid to ice and typically leads to increased particle mass, density, and fall speed (Heymsfield, 1982; Erfani and Mitchell, 2017; Seifert et al., 2019). Although riming can theoretically significantly increase ice water content (IWC) in MPC, it is unclear how much it contributes to ice mass in reality and further to snowfall amounts on the ground with different studies reaching different conclusions (Harimaya and Sato, 1989; Moisseev et al., 2017; Kneifel and Moisseev, 2020; Fitch and Garrett, 2022; Waitz et al., 2022).

Cloud properties are not only determined by the mass and the ratio of liquid and ice particles, but also by their spatial distribution. Observations show that ice particles and liquid droplets in MPC are often mixed heterogeneously leading to the formation of hydrometeor clusters (Korolev et al., 2003; Field et al., 2004; Korolev and Milbrandt, 2022). The ability to quantify spatial scales of IWC clustering would allow for model evaluations beyond comparing distributions of IWC. Additionally, which microphysical processes lead to IWC clustering at which spatial scales is poorly understood. While quantifying spatial scales of cloud particle clusters has been the focus of previous studies, most focused on liquid-phase clouds and analyzed liquid droplet clustering on small scales below 1 m (Kostinski and Shaw, 2001; Shaw et al., 2002; Baker and Lawson, 2010), where turbulence plays a major role in clustering (Wood et al., 2005; Saw et al., 2012a, b). Studies looking at MPC suggest that ice clustering is present at different spatial scales than liquid clusters (Korolev and Milbrandt, 2022; Deng et al., 2024). Deng et al. (2024) propose that ice clusters—defined as regions with enhanced ice particle number or IWC—on larger scales of a few km dominate the inhomogeneity of the ice distribution within clouds. However, their analysis is based on in situ data of a single case over China and it is unclear, if their findings are representative for different types of MPC.

Accurate in situ measurements of IWC remain challenging (Heymsfield et al., 2010; Baumgardner et al., 2017; Tridon et al., 2019), even though in situ cloud probes can provide reliable particle size distribution (PSD) data (Korolev et al., 2013; Moser et al., 2023). Lacking IWC measurements, Deng et al. (2024) calculated IWC from PSD observations assuming that ice particle

mass as a function of ice particle size follows a power law relation . Because deriving size-resolved ice particle densities from in situ PSD alone is not possible yet (to our knowledge), Deng et al. (2024) used constant mass-size parameter from Heymsfield et al. (2010). Therefore, their analyses captures IWC variability due to ice number concentration and size, but not ice particle density, which is commonly linked to riming (Erfani and Mitchell, 2017; Seifert et al., 2019).

Combining collocated cloud radar and in situ PSD data allows to estimate IWC by not only showing great potential to gain better insight on microphysical processes (Nguyen et al., 2022; Mróz et al., 2021), but also to infer ice particle density changes due to riming (Maherndl et al., 2024). This way, IWC variability driven by riming-induced changes in ice particle density can be studied. In recent years, the synergistic employment of both remote sensing and in situ instrumentation during airborne campaigns has become more common (Houze et al., 2017; McMurdie et al., 2022; Nguyen et al., 2022; Kirschler et al., 2023; Sorooshian et al., 2023; Wendisch et al., 2024; Maherndl et al., 2024).

Here, we us collocated cloud radar and in situ cloud probe observations in MPC collected during the IMPACTS (McMurdie et al., 2022) and the HALO-(AC)[3] (Wendisch et al., 2024) aircraft campaigns. The focus of IMPACTS was to study precipitation variability in wintertime snowstorms. The main objective of the HALO-(AC)[3] campaign was studying Arctic air mass transformations. During both campaigns, two aircraft flew in an approximately vertically stacked coordinated pattern to collect spatially and temporally collocated radar and in situ data.

We aim to:

1. Quantify spatial scales of ice clusters in MPC observed during the IMPACTS (mid-latitude winter storms) and HALO-(AC)[3] (Arctic MCAO clouds) aircraft campaigns.

2. Characterize spatial scales at which riming enhances in-cloud ice clustering and link to drivers of riming.

3. Compare ice cluster scales and the impact of riming for mid- and high-latitude MPC.

Because we aim to compare IWC variability in MPC at different latitudes, we are using data from both aircraft campaigns. IMPACTS data was collected during four flights over the US East Coast and the Midwest. For HALO-(AC)[3], We use data from three flights over the Fram Strait west of Svalbard. We compare the contribution of riming to IWC to other ice formation processes absolutely and with respect to the spatial scales of ice clustering using the pair correlation function. The paper is organized as follows: Section 2 introduces the airborne data sets we use to study riming and IWC variability. Section 3 illustrates the methods we use to quantify riming, derive IWC, and analyze scales of IWC variability in clouds. The main results are presented in Sect. 4. In Sect. 5 we summarize and discuss our findings.

2   Data

2.1   Airborne campaigns: IMPACTS and HALO-(AC)[3]

The Investigation of Microphysics and Precipitation for Atlantic Coast-Threatening Snowstorms (IMPACTS, McMurdie et al., 2022) campaign was a NASA-sponsored field campaign to study wintertime snowstorms with a focus on precipitation variabil-

Table 1. Overview of analyzed flight days including campaign, measurement area, and synoptic situation.

Campaign	Flight day	Measurement area	Synoptic situation / mission target
IMPACTS	25 January 2020	East Coast, New York	Warm occluded front
IMPACTS	1 February 2020	East Coast, Atlantic	Warm developing frontal system
IMPACTS	5 February 2020	Midwest	Shallow frontal zone
IMPACTS	7 February 2020	East Coast, Albany	Rapidly deepening cyclone
HALO-(AC)^3	28 March 2022	Fram Strait	MCAO
HALO-(AC)^3	1 April 2022	Fram Strait	MCAO
HALO-(AC)^3	4 April 2022	Fram Strait	MCAO

ity in East Coast cyclones. Here, we use data collected during the winter 2020, where a variety of storms from the Midwest to the East Coast were sampled.

90   The DFG-funded field campaign HALO-(AC)^3 (Wendisch et al., 2024) took place in March and April 2022 and aims at investigating warm air intrusions and cold air outbreaks in the Arctic. In this study, we analyze data collected during MCAO conditions over the Fram Strait west of Svalbard.

Both aircraft campaigns have in common that collocated in situ and remote sensing measurements were conducted with two aircraft. During IMPACTS, the *ER-2* aircraft flew above clouds carrying a variety of passive and active remote sensing

95   instruments including multiple frequency Doppler radars. Simultaneously, the NASA *P-3* aircraft collected measurements of microphysical cloud properties in situ while flying within clouds. During HALO-(AC)^3, the AWI aircraft *Polar 5* and *Polar 6* conducted measurements in a similar manner. *Polar 5*, equipped with a W-band radar among other remote sensing instruments flew above *Polar 6*, which carried out in situ measurements in clouds.

However, both campaigns cover different observation areas and sampled at different frequency rates, i.e., different spatial

100   resolutions. With a typical flight speed of 200 (150) m/s the *ER-2* (*P-3*) covers a larger spatial scale at a coarser resolution than *Polar 5* and *Polar 6*, which flew at 60-80 m/s. While the *ER-2* and *Polar 5* flew at constant altitudes of 20 km and 3 km, respectively, *P-3* and *Polar 6* sampled at different altitudes up to 8.5 and 3 km, respectively. In this study, we investigate data collected during the flight days listed in Tab. 1. We selected these days because of the good collocation (which we define as maximum spatial offsets of 5 km and temporal offsets of 5 min; see Sect. 2.4) between the respective remote sensing and in

105   situ aircraft as well as the data availability. Figure 1 shows all coordinated flight paths.

2.2 Instruments

Equivalent radar reflectivity factor Z_e was measured by multiple radars during IMPACTS: X-band (9.6 GHz, EXRAD, Heymsfield et al., 1996, 2022), Ku and Ka-band (13.6 and 35.6 GHz, HIWRAP, Li et al., 2016, 2022), and W-band (94 GHz, CRS, McLinden et al., 2021, 2022). EXRAD consists of a nadir-pointing and a conically scanning beam, however, we only use the

110   nadir-pointing beam in this study. EXRAD, HIWRAP, and CRS sampled at 4 Hz, 2 Hz, and 4 Hz at vertical resolutions of 19
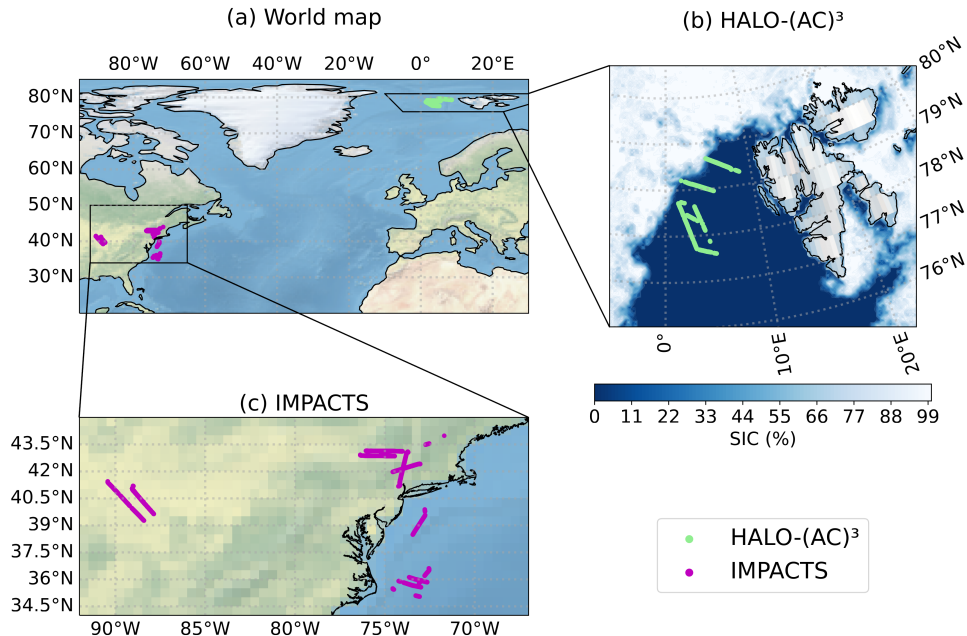
Figure 1. Flight tracks of (a) all analyzed coordinated flight segments, zoomed in on (b) HALO-(AC)³, and (c) IMPACTS measurement area. In (b) the sea ice concentration (SIC) derived from the Advanced Microwave Scanning Radiometer 2 (AMSR2) onboard the GCOM-W1 satellite on 1 April 2022 is shaded in blue.

m, 26 m, and 26 m, respectively. During HALO-(AC)³, a W-band radar (94 GHz, MiRAC-A, Mech et al., 2019; Mech et al., 2024a) was deployed. MiRAC-A was mounted with a 25°backwards inclination, sampled at 1 Hz and Z_e data is available with 5 m vertical resolution. For scattering calculations done within this study, the 25°inclination is negligible (not shown). For both campaigns, Z_e data is quality controlled and corrected for instrument orientation and aircraft motion (for MiRAC-A, see Mech

115 et al., 2019). Uncertainties of Z_e stemming from radar calibration are estimated to be below 1 dB and 0.5 dB for IMPACTS and HALO-(AC)³ data, respectively (Finlon et al., 2022; Mech et al., 2019). MiRAC-A Z_e is corrected for attenuation due to liquid water content (LWC) as described in Maherndl et al. (2024); CRS Z_e as described in Finlon et al. (2022). Attenuation due to water vapor and atmospheric gases is below 0.5 dB for all radars and therefore neglected.

During HALO-(AC)³, brightness temperature T_B measurements at 89 GHz were collected and are used to derive the LWP.

120 Differences in T_B for clear-sky and cloudy situations are used to retrieve LWP over ocean via a regression approach (Ruiz-Donoso et al., 2020; Maherndl et al., 2024). Lidar measurement of backscattered intensities at 532 nm (parallel and perpendicular polarized) and 355 nm (not polarized; Stachlewska et al., 2010) are used to derive cloud top height (CTH) during HALO-(AC)³ (Mech et al., 2022a; Schirmacher et al., 2023; Maherndl et al., 2024; Mech et al., 2024b).

Cloud particle observations obtained with a variety of cloud probes cover a size range from 2 μm to about 2 cm for IMPACTS

125 and 2.8 μm to 6.4 mm for HALO-(AC)³. For IMPACTS, we use data from a Fast-Cloud Droplet Probe (Fast-CDP, 2-50 μm,

Lawson et al., 2017), a Two-Dimensional Stereo (2D-S, Lawson et al., 2006) probe (10-2000 µm, pixel resolution of 10 µm), one horizontally, and one vertically oriented High Volume Precipitation Spectrometer, version 3, (HVPS-3, Lawson et al., 1998) probe (0.3-19.2 mm, pixel resolution of 150 µm). For HALO-(AC)[3], we use data from a Cloud Droplet Probe (CDP, 2.8-50 µm, Lance et al., 2010), a Cloud Imaging Probe (CIP, 15-960 µm, pixel resolution of 15 µm, Baumgardner et al., 2001), and a Precipitation Imaging Probe (PIP, 103-6400 µm, pixel resolution of 103 µm, Baumgardner et al., 2001). Here, we use merged particle size distribution (PSD) data from the respective campaign (Bansemer et al., 2022; Moser et al., 2023), which are derived from the instruments listed above. As in Moser et al. (2023) and Maherndl et al. (2024), we assume all particles larger 50 µm in MPC to be ice crystals. As in Maherndl et al. (2024), we only include data up to -1 °C to avoid melting effects. In addition, we manually looked through in situ images of all analyzed flight segments and removed two IMPACTS segments, where we could identify supercooled droplets larger 50 µm. LWC was measured in situ with a King probe (King et al., 1978) and a Nevzorov probe (Korolev et al., 1998; Lucke et al., 2022; Lucke et al., 2024) during IMPACTS and HALO-(AC)[3], respectively. Due to poor data availability[1] and high uncertainties of IWC measurements, IWC is calculated from the PSD as described in more detail in Sect. 3.2. For more detail on IMPACTS and HALO-(AC)[3] instrumentation and data processing, we refer the reader to McMurdie et al. (2022) and Moser et al. (2023), Mech et al. (2022a), as well as Maherndl et al. (2024), respectively.

2.3 Synoptic situation

In this section, we give a brief overview of the "typical" synoptic situations encountered during the different field campaigns to provide context on the types of MPC that we analyze. We use one example flight segment for each campaign, which we describe in detail in Sect. 4.1.1 and 4.1.2.

During IMPACTS, observations of a variety of mid-latitude wintertime storms in different development stages were conducted. The focus was on observing banded precipitation structures. Observations range from a relatively weak and warm developing Atlantic low systems without major banding structures (1 February 2020) to rapidly deepening cyclones with significant snowfall and snowbands (5 February 2020). The majority of measurements stem from the U.S. Midwest, and close to the East Coast (both over ocean and land) ranging up to southern parts of Canada (Fig. 1). The coordinated *ER-2* and *P-3* flights on 5 February sampled an elevated warm front over shallow, pre-existing cold air as a low pressure center developed over Louisiana and Mississippi. The developing circulation around the low produced a low-level northeasterly flow across the Midwest. Due to the overrunning warm moist air from the south, precipitation in the form of rain (to the south) and snow (to the north) formed. During the period of observations, snowband structures were observed.

Measurements during HALO-(AC)[3] were conducted west of Svalbard over both open ocean and sea ice. However, clouds were very thin to non-existent over sea ice during all three flights used here. Northerly to northeasterly flow brought cold air masses from the sea ice of the higher Arctic to the comparatively warm open ocean. This led to the formation of roll cloud streets. During 1 April 2022 the MCAO was especially strong meaning the difference of the potential at sea surface and the

---

[1]IMPACTS (2020): Water Isotope System for Precipitation and Entrainment Research (WISPER, Toohey et al., 2022) data product is available but unreliable under riming / icing conditions; HALO-(AC)[3]: Nevzorov probe data product only for April flights

potential temperature at 850 hPa was large (about 8 K), while during 28 March and 4 April 2022 weaker MCAO conditions were observed due to air masses being convected from North America over Siberia (28 March) or the central Arctic (4 April)
160 to Svalbard (Walbröl et al., 2024).

2.4 Collocation

To combine in situ and remote sensing observations of the two aircraft, we use the same collocation criterion as in Maherndl et al. (2024), which is also extended to the IMPACTS data. To summarize, the nearest radar data point to the in situ measurements is selected following Chase et al. (2018) and Nguyen et al. (2022). Each 1 Hz, 2 Hz, or 4 Hz radar aircraft (*Polar 5* and
165 *ER-2*) data point is matched with the spatially closest in situ aircraft (*Polar 6* and *P-3*) data point within a 5 min time window. We consider data with maximum spatial offsets of 5 km as "collocated". The closest radar range gate to the flight altitude of the in situ aircraft is chosen. Averaging over certain height ranges did not lead to significant improvements.

Rolling averages were applied to Z_e and in situ data to obtain more robust statistics for the latter. To cover approximately the same spatial scales, averaging windows of 10 s and 30 s are chosen for IMPACTS and HALO-(AC)^3, respectively. With
170 typical flight speeds of 180-200 m/s and 60-80 m/s during IMPACTS and HALO-(AC)^3, respectively, this corresponds to spatial scales of 1.8-2.0 km and 1.8-2.4 km. We assume the in situ measurement is representative of the entire matched radar volume. Possible implications of this assumption on the riming retrieval are discussed in Maherndl et al. (2024).

3 Methods

3.1 Retrieving ice particle riming

175 We use the normalized rime mass M (Seifert et al., 2019) to describe riming. M is defined as the particle's rime mass m_{rime} divided by the mass of a size-equivalent spherical graupel particle m_g, where we assume a rime density of $\rho_{rime} = 700 \ \mathrm{kg \ m^{-3}}$:

$$M = \frac{m_{\mathrm{rime}}}{m_g} \tag{1}$$

where

180 $$m_g = \frac{\pi}{6} \rho_{\mathrm{rime}} D_{\mathrm{max}}^3. \tag{2}$$

The maximum dimension D_{max} is defined as the diameter of the smallest circle encompassing the cloud particle in m and is used to parameterize particle sizes.

We retrieve M using the two methods introduced in Maherndl et al. (2024), which are termed the *combined method* and the *in situ method*. The methods in Maherndl et al. (2024) were developed for HALO-(AC)^3, but we apply them to IMPACTS
185 data with slight adjustments due to different instrumentation. In the following, we give a brief explanation of both methods and describe the adjustments for IMPACTS data. For more detail, we refer the reader to Maherndl et al. (2024).

7

The combined method derives M along the flight track of the in situ airplane from collocated PSD and radar reflectivity Z_e measurements. It therefore relies on collocated in situ and remote sensing flights. An Optimal Estimation (Rodgers, 2000) algorithm is used to retrieve M by matching simulated radar reflectivities Z_e obtained from observed in situ PSD with the spatially and temporally closest measured Z_e. As forward operator we use the Passive and Active Microwave radiative TRansfer tool (PAMTRA, Mech et al., 2020) which includes empirical relationships Maherndl et al. (2023a) for estimating particle scattering properties as a function of M. For IMPACTS, the combined method is applied (separately) to X-, Ku-, Ka- and W-band Z_e (see Sect. 4.1.3). As in Maherndl et al. (2024), we use the riming dependent mass-size parameter relation for dendrites from Maherndl et al. (2023a) that were estimated for different degrees of riming, i.e., M values. Dendrites were chosen, because 86.2 % of data during the analyzed IMPACTS segments are within temperature ranges of -20 °C to -10 °C and -5 °C to 0 °C, where plate-like growth of ice crystals is preferred (only 13.8 % of the data lie between -10 °C and -5 °C, where column-like growth dominates). We assume dendrite shapes for the whole dataset, because of two reasons. First, Maherndl et al. (2024) found assuming plates or dendrites gives the same results within uncertainty estimates, and second, we want to keep the analysis of IMPACTS and HALO-(AC)[3] data as consistent as possible.

The in situ method uses in situ measurements of ice particle area A, perimeter P, and $D_{\max}$ to derive M for individual ice particles from which an average M for the particle population is derived. The in situ method is applied to 2D-S and HVPS-3 data for IMPACTS as was done using CIP and PIP data for HALO-(AC)[3] in Maherndl et al. (2024). P and A measurements in pixel are used to calculate complexity $\chi = \frac{P}{2\sqrt{\pi A}}$. Simulated rimed aggregates from Maherndl et al. (2023b) are used to derive empirical functions relating χ and $D_{\max}$ to M, where χ and $D_{\max}$ are derived using the same processing steps as for the respective cloud probes. Because these processing steps were slightly different for 2D-S and HVPS-3 operated during IMPACTS[2] than for CIP and PIP during HALO-(AC)[3], new fit functions (based on 18352 simulated dendrites; with $R^2 = 0.92$) had to be derived for IMPACTS:

$$\log_{10}(M) = \frac{1.11 - \chi + 0.00141 \cdot D_{\max}}{0.00432 \cdot D_{\max} + 0.218}. \tag{3}$$

Only a subset of ice particles can be used to derive M with the in situ method, because particles cannot touch edges to derive P and need to be large enough to derive meaningful χ. We therefore assume the combined method—which uses the full PSD—gives more reliable results when the aircraft are reasonably collocated. In situ method results are therefore only shown in Sect. 4.1.1 and 4.1.2 as references and the combined method is used in all further analysis steps.

3.2 Deriving ice water content (IWC)

IWC is calculated by summing the product of ice particle mass $m(D_{\max})$ and $N(D_{\max})$ for the probes' lower to upper size ranges D_{lower} to D_{upper}

$$IWC = \sum_{D_{lower}}^{D_{upper}} m(D_{\max})N(D_{\max})\Delta D_{\max}, \tag{4}$$

---

[2]The number of perimeter pixel P is computed by the sum of all pixel that are eroded when applying a "+" shaped erosion kernel without performing dilation/erosion sequences as was done during HALO-(AC)[3].

where $\Delta D_{\max}$ is the size bin width. $m(D_{\max})$ is approximated by a power law relation with prefactor a_m and exponent b_m

$$m(D_{\max}) = a_m D_{\max}^{b_m}. \tag{5}$$

a_m scales the density of ice particles (independent of particle size) and b_m modulates the size dependency of particle mass, which is related to particle shape and growth processes. a_m and b_m depend strongly on riming (e.g., Mitchell, 1996) and reported literature values range from 0.0058 to 466 for a_m and 1.8 to 3.0 for b_m in SI units (e.g., discussed by Mason et al., 2018). As shown by Maherndl et al. (2023a), a_m and b_m strongly depend on the amount of riming, which increases particle densities. Maherndl et al. (2023a) provide a_m and b_m values for discrete M, which are interpolate to obtain parameters for a continuous M in this study. We derive a_m and b_m for each time step as a function of the retrieved M. IWC is then calculated with Eq. 4 for each time step based on the measured PSD and the derived a_m and b_m parameters. We refer to this quantity as IWC_r (IWC accounting for riming).

To estimate the contribution of the riming process to IWC, we also calculate IWC using fixed mass-size parameters a_m and b_m for unrimed particles (also taken from Maherndl et al., 2023a), thereby neglecting density changes (e.g., due to riming). We refer to this quantity as IWC_u. IWC_u can be seen as the "theoretical" IWC, if the ice particles were unrimed so that the riming contribution can be estimated from the difference between IWC and IWC_u. However, this implies that riming does not impact the size of the unrimed ice particle, which is not necessarily the case in nature. Riming typically not only leads to an increase in ice particle density, but also ice particle size (Seifert et al., 2019). Therefore, we likely underestimate the contribution of riming to particle mass when comparing IWC_u with IWC. Since we are interested in the contribution of riming to IWC variability, this approach likely results in a conservative estimate of the contribution of riming to IWC variability.

3.3 Characterizing scales of IWC variability in clouds

Similar to Deng et al. (2024), we use the pair correlation function (PCF) to quantify the spatial inhomogeneity of ice water in the observed clouds. In discrete systems, the PCF describes the degree of deviation from the homogeneous Poisson process. In clouds, the PCF can be used to quantify the degree of clustering or variability of a certain parameter such as the number concentration of liquid droplets, the number concentration of ice particles, LWC, or IWC (e.g., Shaw et al., 2002; Saw et al., 2012a; Deng et al., 2024). The PCF applied to a one-dimensional parameter p is given by:

$$\eta(r) = \frac{\overline{p(0)p(r)}}{(\overline{p})^2} - 1, \tag{6}$$

where $p(0)$ is the parameter at a given point, $p(r)$ the parameter at the lag r from that point, and $\overline{p}$ the average of p (Kostinski and Jameson, 2000; Shaw et al., 2002). Thus, $\eta(r)$ is a measure for the probability to find clusters of p as a function of lag r compared to $\overline{p}$. Positive values indicate the occurrence of clusters and the higher $\eta(r)$ the higher the probability to find clusters at that scale. If p follows a homogeneous Poisson distribution, which PCF assumes to be statistically homogeneous, $\eta(r) = 0$. Negative values indicate that at the given scale, it is less likely to find clusters than on average over the whole segment.

In this study, only straight flight segments with a minimum of 200 s of continuous in-cloud measurements are used to calculate $\eta(r)$. The respective radar sensitivity limits are used to define "in-cloud". We allow measurement gaps with a maximum

length of 5 s, which are linearly interpolated. Table 2 gives an overview of all segments we analyze including duration and data amount. Because IWC is derived using running averages of 10 s and 30 s for IMPACTS and HALO-(AC)[3] data, respectively, we investigated the impact of the window size of the moving average on $\eta(r)$. We found that while increasing the window size from 1 s to 10 (30) s for IMPACTS (HALO-(AC)[3]) decreases absolute values of $\eta(r)$, at which lags r $\eta(r)$ is positive does not change (not shown). This is because applying a moving average smooths peaks in the 1 Hz signal, but does not necessarily change their periodicity as long as the window size is reasonably small.

Additionally, we use power spectra in order to gain insight on scales of variability of CTH and LWP during HALO-(AC)[3]. To do so, each data segment is mean-centered and linearly detrended. To minimize edge effects, a Hann window is applied to each segment. Frequency is converted to wavelength using the aircraft speed v_{air}. With a minimum time range of 200 s per segment, we capture spatial scales of 12 km for HALO-(AC)[3] meaning that we do not capture synoptic-scale motions. We interpret results up to 0.1 Hz meaning spatial scales of 600 m.

Figure 2 visualizes the PCF and power spectra for synthetic data. In the case of a homogeneous Poisson process (Fig. 2a), $\eta(r) = 0$ (Fig. 2d) and the power spectral density shows no significant peaks (Fig. 2g). For a periodic sine function with added Poisson noise (Fig. 2b), $\eta(r)$ is positive for small lags and oscillates around 0 for larger lags with peaks occurring at multiples of the wavelength λ of the sine function (Fig. 2e). The power spectrum shows a peak at λ (Fig. 2h). If the modulus function is applied to the sine (Fig. 2c), $\eta(r)$ (Fig. 2f) is smaller than in Fig. 2e due to the lower signal to noise ratio and the oscillation occurs at $\lambda/2$. The power spectrum also shows a peak at $\lambda/2$ (Fig. 2i).

4 Results and discussion

To characterize the influence of riming on the spatial variability of ice clusters in clouds, we first need to know the amount of riming as well as its impact on IWC and second, we need to know spatial IWC cluster scales with and without riming. Therefore, this section is structured as follows. First, we quantify the amount of riming observed during the two analyzed campaigns (Sect. 4.1). Then, we show that the retrieved amounts of riming have a significant impact on IWC (Sect. 4.2). Finally, we quantify in-cloud IWC variability (Sect. 4.3) and discuss the impact of riming on spatial scales and probability of IWC clusters in clouds.

4.1 Riming occurrence

MPC properties, synoptic situations (Sect. 2.3), and measurement locations (Fig. 1) vary between IMPACTS and HALO-(AC)[3]. Clouds during collocated IMPACTS segments have much larger vertical extents than during HALO-(AC)[3]. The median CTH during IMPACTS segments is 7.3 km (25-75 % quantile range: 6.3-7.8 km). Here, we define CTH as the height of the highest radar range gate with continuous Z_e above the in situ aircraft altitude. Clouds observed during collocated HALO-(AC)[3] segments were predominately shallow roll clouds that formed during MCAOs. The maximum CTH during all segments was 2.2 km (25-75 % percentile range: 0.69-1.1 km). Cloud properties during 1 and 4 April are described in detail in Schirmacher, et al. (2024).

Table 2. Overview of analyzed segments including campaign, flight day, start and end times in UTC, and number of 1 s data points.

Campaign	Flight day	Segment start	Segment end	Number of data points
IMPACTS	25 January 2020	20:30:37	20:40:04	568
IMPACTS	25 January 2020	21:08:31	21:17:16	526
IMPACTS	25 January 2020	21:41:01	21:53:38	758
IMPACTS	1 February 2020	13:08:48	13:16:47	480
IMPACTS	1 February 2020	14:35:24	14:39:32	249
IMPACTS	5 February 2020	21:05:28	21:10:57	330
IMPACTS	5 February 2020	21:15:47	21:19:27	221
IMPACTS	5 February 2020	21:20:56	21:28:27	452
IMPACTS	5 February 2020	21:49:52	22:04:07	856
IMPACTS	5 February 2020	23:07:26	23:12:40	315
IMPACTS	7 February 2020	15:12:42	15:20:23	462
IMPACTS	7 February 2020	15:35:00	15:48:47	828
IMPACTS	7 February 2020	15:57:02	16:08:11	670
HALO-(AC)^3	28 March 2022	14:10:44	14:18:43	480
HALO-(AC)^3	28 March 2022	14:20:20	14:25:16	287
HALO-(AC)^3	28 March 2022	14:35:07	14:39:33	267
HALO-(AC)^3	28 March 2022	14:41:26	14:45:16	331
HALO-(AC)^3	1 April 2022	11:08:38	11:18:59	622
HALO-(AC)^3	1 April 2022	11:20:38	11:33:02	745
HALO-(AC)^3	1 April 2022	12:07:18	12:14:14	417
HALO-(AC)^3	1 April 2022	12:15:54	12:20:56	303
HALO-(AC)^3	1 April 2022	12:24:57	12:33:38	522
HALO-(AC)^3	1 April 2022	12:34:03	12:39:09	307
HALO-(AC)^3	4 April 2022	11:48:05	12:00:12	728
HALO-(AC)^3	4 April 2022	13:11:48	13:18:24	397
HALO-(AC)^3	4 April 2022	13:19:14	13:30:22	669

In the following, we give a brief overview on differences in MPCs encountered during the two campaigns using two "typical" example cases. We show a flight segment from 5 February 2020 for IMPACTS (Sect. 4.1.1), and from 1 April 2022 for HALO-(AC)^3 (Sect. 4.1.2). We present M, retrieved with combined and in situ method, and discuss uncertainties. Then, we extend to data from all collocated segments (Sect. 4.1.3).
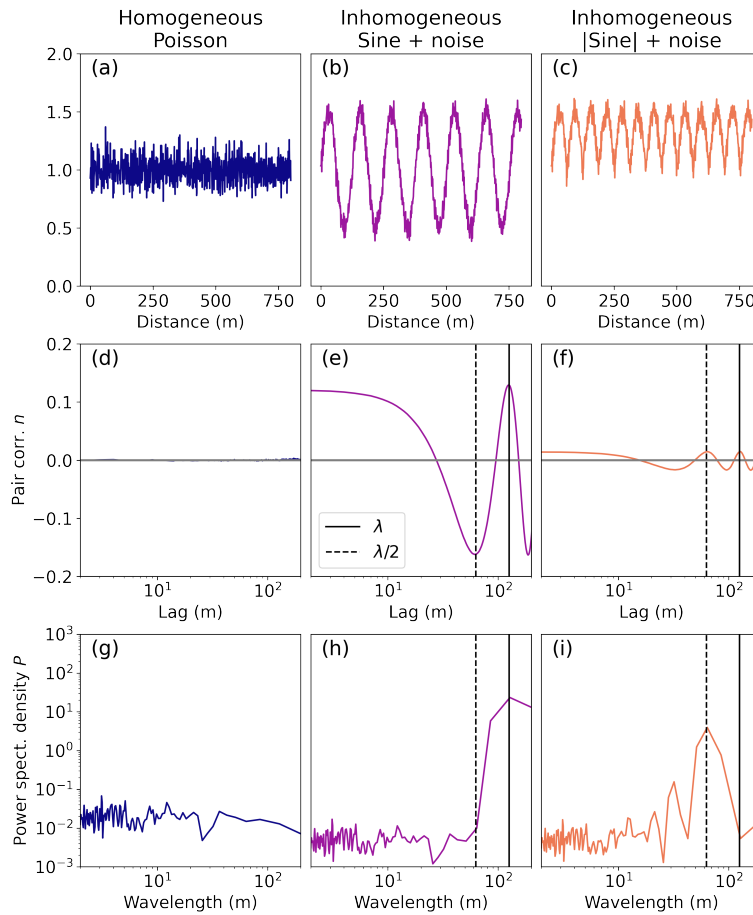
Figure 2. Schematic diagram introducing the pair correlation function (PCF) and power spectral density for (a) a homogeneous Poisson distributed signal, (b) a sine curve with wavelength λ and added Poisson noise, and (c) the same sine curve but mirrored upwards along $x = 1$ to show the impact of λ and signal-to-noise ratio. The respective PCF η as a function of lag is shown in (d)-(f); the power spectra density as a function of wavelength in (g)-(i). The solid and dashed lines indicate λ and $\lambda/2$ of the sine curve in (b).

4.1.1 Case study 1: Mid-latitude winter storm on 5 February 2020

Figure 3 shows a 64 km segment from 5 February, where *ER-2* and *P-3* were sampling a developing low pressure system over Illinois from 23:07:26 to 23:12:40 UTC. According to the level-2 MODIS cloud product (NASA worldview), the cloud top temperature (CTT) was -33 ± 5 °C. W-band Z_e shows the deep cloud with convective cell structures near cloud top from which sheared fall streaks stretch down (Fig. 3a). *P-3* measured number of ice particles larger than 50 μm N_i in the range 910 m^3 to 2800 m^3 (Fig. 3b). Here we show D_{32} (Fig. 3b), which is the proxy for the mean mass-weighted diameter (e.g., Maahn et al., 2015). D_{32} is defined as the ratio of the third to the second measured PSD moments (e.g., Mitchell, 1996). During the first 20 km of the segment, ice particles had D_{32} of about 3 mm and were lightly rimed with M of about 0.02 (Fig. 3.c).

12

Afterwards, D_{32} increases up to 8 mm, indicating aggregates and M drops below the riming threshold of 0.01. From $-88.9°$E onward, D_{32} decreases and M increases. Combined method M results using the different frequencies show good agreement between X-, Ku-, and Ka-band. W-band results are likely biased high due to the high D_{32} as will be discussed in Sect. 4.1.3. IWC is calculated with Eq. 4 using (1) the measured PSD and mass-size parameters a_m and b_m for unrimed particles (blue line) and (2) a_m and b_m based on look up tables (Maherndl et al., 2023a) for each time step depending on retrieved M for each frequency (black lines). The derived IWC from Ku-band M varies between 0.015 $\mathrm{gm^{-3}}$ and 0.31 $\mathrm{gm^{-3}}$(panel 4). If riming is neglected, i.e., mass size parameter for unrimed particles are used in the IWC calculation, IWC is on average a factor of 3.7 lower.

The increase in M starting at -88.7°E could be linked to the decrease in CTH (as seen by the radar). Some particles are possibly rimed in liquid layers near cloud top and fall down to the measurement location. On their way down, they might undergo additional growth processes (condensational growth or aggregation) leading to a decrease of M, since M is normalized to particle size. However, King probe measurements show that liquid water also occurs at the *P-3* position. Therefore additional riming can take place at the *P-3* location and possibly in cloud layers above. 2-DS images (Fig. 3) show a change from large, lightly rimed aggregates to small, more heavily rimed particles.

4.1.2 Case study 2: Arctic roll clouds on 1 April 2022

Figure 4 shows a 35 km segment from 1 April, where *Polar 5* and *Polar 6* were sampling perpendicular to the roll cloud structures formed during a MCAO over the Fram Strait from 11:20:38 UTC to 11:33:02 UTC (see Maherndl et al., 2024, for a detailed discussion of the case as well as particle images). The MODIS CTT was -18 ± 5 °C. W-band Z_e shows the vertical structure of the individual cloud rolls (Fig. 4a). While *Polar 6* was flying close to cloud top, N_i was high with a maximum of 27300 $\mathrm{m^{-3}}$, while D_{32} was low with a minimum of 0.077 mm (Fig. 4b). Once *Polar 6* was descending, N_i dropped to a minimum of 4600 $\mathrm{m^3}$, while D_{32} increased up to 1.4 mm (panel 2). M oscillates between 0.01 and 0.1, with peaks occurring in streaks of high Z_e (Fig. 4c). The resulting IWC is between 0.022 $\mathrm{gm^{-3}}$ and 0.084 $\mathrm{gm^{-3}}$. This is a factor 2.8 higher compared to using a mass-size parameterization for unrimed particles (Fig. 4d).

Both methods used to derive M agree well for this segment in terms of M distributions and location and extent of maxima ($R^2 = 0.52$). Statistical agreement between both methods was achieved during all HALO-(AC)[3] segments used in this study. However, spatio-temporal agreement could not be achieved for inhomogeneous cloud observations (e.g., when *Polar 6* was flying in and out of cloud close to CTH) as discussed in Maherndl et al. (2024).

4.1.3 Campaign overview

In the previous section, two case studies were used to show differences between clouds observed during the two campaigns, especially in terms of vertical extent, structure, and riming. In spite of these differences, normalized rime mass M distributions derived for IMPACTS and HALO-(AC)[3] are similar (Fig. 5a, b). Median M for all collocated IMPACTS segments are 0.024, 0.022, 0.025, and 0.034 when derived with X, Ku, Ka, and W-band Z_e, respectively. During collocated HALO-(AC)[3] segments, median M is 0.024. For IMPACTS, the disagreement of the W-band results to the other frequency bands is due
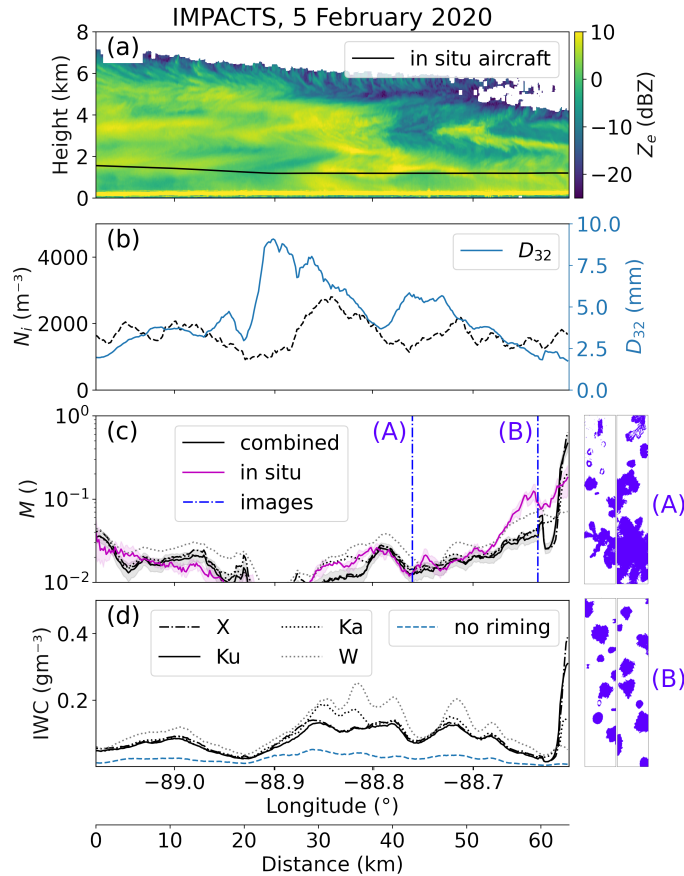
Figure 3. Collocated flight segment from 5 February 2020 at 23:07:26 to 23:12.40 UTC during IMPACTS. (a) W-band radar reflectivity Z_e, and *P-3* flight altitude; (b) ice number concentration N_i and mass-weighted diameter D_{32} derived from the 10 s running averaged particle size distribution (PSD); (c) normalized rime mass M from combined (black) and in situ method (magenta) including uncertainty estimates (combined: optimal estimation (OE) standard deviation, in situ: 10 s running standard deviation), where the combined method was applied to X-, Ku-, Ka-, and W-band Z_e (Ku-band results, which are used in the further analysis, are shown as solid lines); (d) ice water content (IWC) derived from the 10 s running averaged PSD and combined method M (black) and assuming $M = 0$ (blue). Combined method results for different radar frequencies are drawn as dashed lines. 2-DS images at (A) -88.78°E and (B) -88.69°E are shown in blue next to panels (c) and (d).

to the occurrences of large ice particle sizes. Due to saturation effects for Z_e values associated with large particles at 94 GHz, the riming-dependent parameterization (Maherndl et al., 2023a) used here has a positive Z_e bias for size parameters $x = 2\pi\alpha_e D_{max}/\lambda > 4$ where $x > 4$. Here α_e is the ice particle's effective aspect ratio, and λ the radar wavelength. The positive Z_e bias for $x > 4$ results in a positive bias of M. For IMPACTS, 25% of data have $D_{32} > 3.2$ mm which corresponds 330 to $x = 4$ at 94 GHz assuming a typical value of $\alpha_e = 0.6$. Therefore W-band results for IMPACTS are not as trustworthy as the other wavelengths and are not used in the following analysis. Different to IMPACTS, the M bias is negligible for HALO-
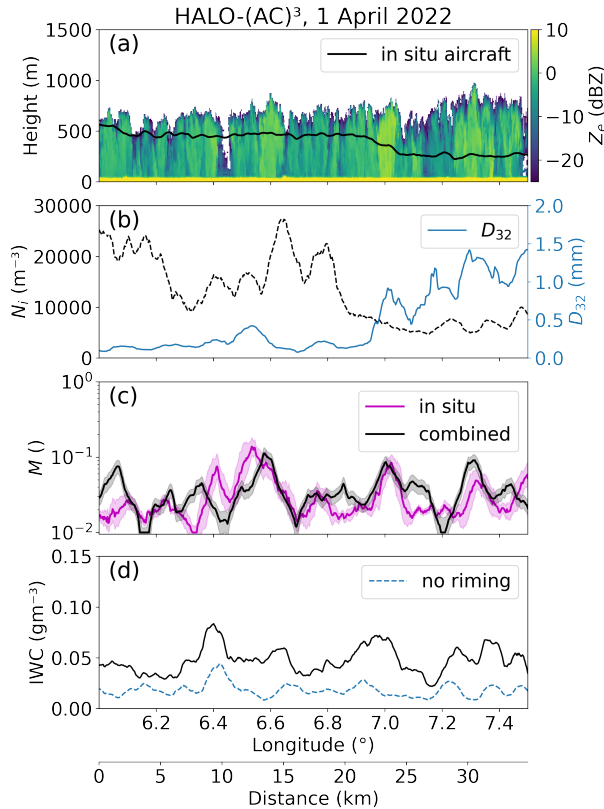
Figure 4. As in Fig. 3 but for the collocated flight segment from 1 April 2022 11:20:38-11:33:02 UTC during HALO-(AC)^3. Only W-band radar reflectivities are available.

(AC)^3 due to the smaller particle sizes and $D_{32} < 3.2$ holds for 90% of the data. In Appendix A, an overview of microphysical parameters during each analyzed segment is given.

4.2 Sensitivity study

335 To motivate our further analysis and to evaluate whether the retrieved amounts of riming significantly impact IWC, we conduct a sensitivity study.

We assume that $N(D_{\max})$ follows a modified gamma distribution and use the normalized form introduced by Delanoë et al. (2005, 2014) and extended by Maahn et al. (2015) for the maximum dimension $D_{\max}$

$$N(D_{\max}) = N_0^* \frac{(b_m + \mu + 1)^{b_m + \mu + 1} \Gamma(b_m + 1)}{\Gamma(b_m + \mu + 1)(b_m + 1)^{b_m + 1)}} \left(\frac{D_{\max}}{D_m}\right)^{\mu} e^{-(b_m + \mu + 1)D_{\max}/D_m}, \tag{7}$$

340 where N_0^* is the overall scaling parameter, μ the shape parameter, and D_m is the "mass-weighted" scaling parameter for the particle size. We vary N_0^* and D_m—which can be calculated from PSD moments (see Maahn et al., 2015)—based on 10 to 90% quantile values derived from all measured PSDs during IMPACTS. Exclusively IMPACTS data was chosen, because

15
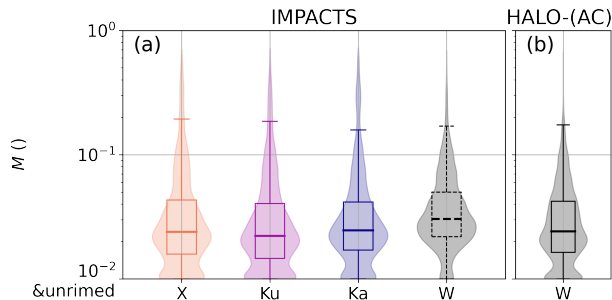
Figure 5. Box plots and superimposed violin plots showing normalized rime mass M results obtained from a closure of collocated radar reflectivity Z_e and in situ particle size distribution ("combined method" from Maherndl et al. (2024)) for radar reflectivities available during (a) IMPACTS and (b) HALO-(AC)[3]. W-band results during IMPACTS are dashed due to biases (see text). $M < 0.01$ are plotted at 0.01 to be visible on the logarithmic scale.

larger particles and higher number concentrations were measured during IMPACTS than during HALO-(AC)[3]. μ is varied from 0 to 64 based on extreme values reported in the literature (Tridon et al., 2022). M is varied from 0.005 to 1, which correspond to the 10 % quantile of M retrieval results from both campaigns and the maximum "physical" M based on its definition.

We find that although median M are below 0.03 for both campaigns, even small amounts of riming—or rather changes in ice particle density—can result in large changes of IWC. Figure 6 shows IWC calculations assuming gamma PSDs with varying N_0^* (left column) and M (right column) as a function of D_m. Similar to Maahn and Löhnert (2017), we find the shape parameter μ does not impact IWC or Z_e significantly and therefore only $\mu = 0$ is shown. D_m, which can be seen as a proxy for particle size, has the largest impact on IWC. By changing D_m from 1 to 8 mm, IWC changes by three orders of magnitude. IWC increases by about one order of magnitude, when N_0^*—the proxy for total number concentration of particles—is increased by one order of magnitude. Depending on D_m, varying M can result in IWC changes up to two order of magnitudes. When only considering M values encountered during the analyzed campaigns, the change in IWC reaches one order of magnitude.

To show the impact of riming on radar reflectivity Z_e, which can be seen as a proxy for IWC, we conduct a sensitivity study for Ku and Ka-band Z_e. In doing so, we aim to highlight the importance of accounting for riming in radar retrievals. Z_e is forward simulated using the same PSDs with PAMTRA assuming a temperature of $-10\,°C$. Particle scattering is parameterized with the riming-dependent parameterization (Maherndl et al., 2023a). X-band is not shown due to being nearly identical to Ku-band; W-band is not shown due to the riming-dependent parameterization bias for large D_m at W-band (see Sect. 4.1.3). Varying M within observed ranges results in Z_e changes of up to 20 dB depending on D_m for both Ku- and Ka-band, albeit with slightly larger spread at Ka-band. Similar to Fig. 6, varying D_m results in the largest Z_e changes. Observed ranges of M result in larger Z_e changes than observed ranges of N_0^*. Therefore in our data set, Z_e depends more heavily on riming than on number concentration.

We therefore conclude that for the range of M observed during HALO-(AC)[3] and IMPACTS, the effect of riming on IWC should not be neglected to avoid biases up to one order of magnitude for IWC.
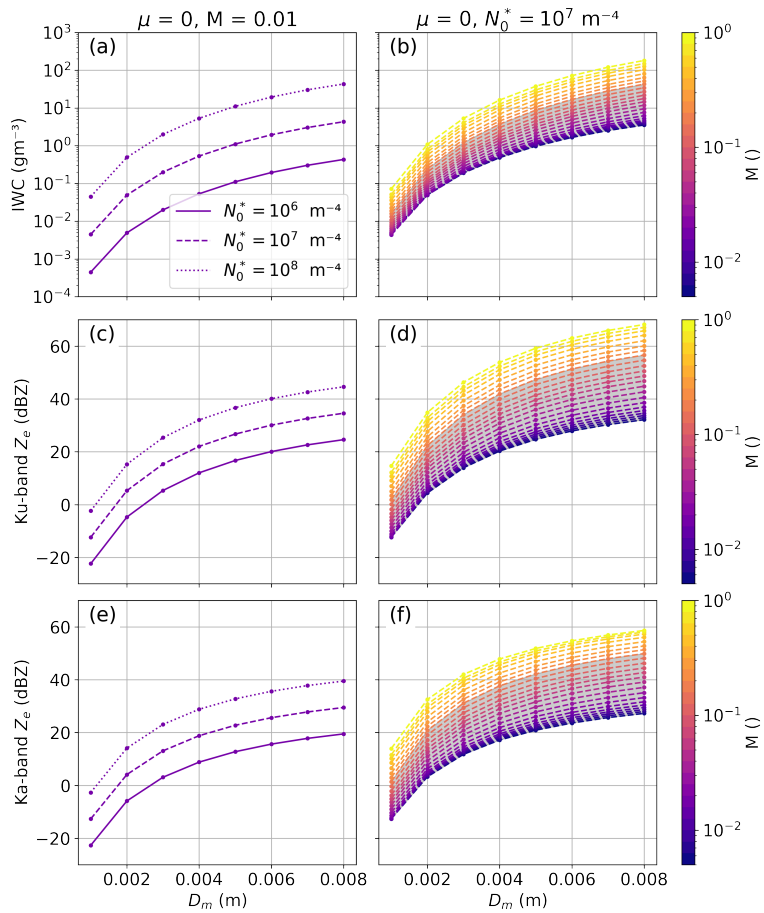
Figure 6. Ice water content (IWC) (top), Ku-band Z_e (middle), and Ka-band Z_e (bottom) calculated from gamma particle size distributions as functions of D_m parameter. Results for varying N_0^* parameter are shown as solid and dashed lines in (a), (c), (e); for varying normalized rime mass M are color-coded in (b), (d), (f). Shaded areas in (b), (d), (f), (h) indicate M ranges observed during IMPACTS (90 % range: $0.005 < M < 0.15$).

4.3 Quantifying in-cloud IWC variability with and without riming

Because even small amounts of riming significantly impact IWC, we evaluate differences in IWC variability when accounting for riming vs. when neglecting riming in the following. As described in Sect. 3.2, IWC is calculated with Eq. 4 based on the measured PSD and (1.) using mass-size parameters a_m and b_m for unrimed particles (IWC$_u$) and (2.) varying a_m and b_m for each time step as a function of the retrieved M (IWC$_r$). During all analyzed IMPACTS flight segments, rime mass (IWC$_r$ − IWC$_u$) makes up 68.6 / 65.7 / 68.8 % of IWC$_r$ based on X- / Ku- / Ka-band results. During HALO-(AC)³, rime mass makes up 62.7 %.

Figure 7 shows the average PCF η over all analyzed IMPACTS and HALO-(AC)^3 segments for N_i (Fig. 7 first column), IWC$_r$, and IWC$_u$ (Fig. 7 second column). To visualize the difference between IWC$_r$ and IWC$_u$, Fig. 7, 3rd column shows the $\eta_{IWC_r} - \eta_{IWC_u}$. By this, we can isolate the contribution of the riming process to IWC. Positive values of $\eta_{IWC_r} - \eta_{IWC_u}$

375   indicate riming increases the variability of IWC clusters at the given lag while negative values are related to riming smoothing out IWC variability. Because we are interested at which spatial scales riming influences IWC variability, we only discuss the differences larger than zero.

Both in terms of N_i and IWC, IMPACTS segments have higher η on average than HALO-(AC)^3 segments meaning N_i and IWC have more variability on the investigated spatial scales (Fig. 7a, b). Note that both quantities are calculated from running

380   PSD averages of 10 s and 30 s for IMPACTS and HALO-(AC)^3, respectively, to cover similar spatial scales (about 1.8 km) given the different flight speeds. The smaller count of data points averaged for IMPACTS might lead to higher variability. However, computing η for 30 s running averages results in similar curves with close to the same lags where $\eta = 0$, and slightly lower η, yet still higher than for HALO-(AC)^3 (not shown).

During IMPACTS, variability occurred at larger spatial scales than during HALO-(AC)^3 as indicated by positive η at larger

385   lags (Fig. 7a, b). Differences between η for N_i and IWC indicate ice growth processes play a large role for IWC variability in addition to ice formation processes. For both campaigns, $\eta > 0$ for IWC is shifted to larger spatial scales than for N_i indicating ice growth processes lead to increased variability at large spatial scales. For IMPACTS, accounting for riming shifts scales of IWC variability to slightly smaller lags and increases η significantly at small lags, meaning riming increases IWC variability at lags < 5 km (Fig. 7c). For HALO-(AC)^3, riming leads to IWC variability at lags below 1 km as well as between 3-5 km. (Fig.

390   7c) However, differences between η_{IWC_r} and η_{IWC_u} are smaller than for IMPACTS.

4.3.1 Dependency on particle size

To identify which size range of particles contributes most to N_i and IWC variability, we split the PSD into small ($50 < D_{max} < 300$ μm), medium ($300 < D_{max} < 900$ μm), and large ($D_{max} > 900$ μm) particle sizes to calculate N_i and IWC (Fig. 7d-i). For IMPACTS, the probability of small particle N_i (IWC) clusters is higher than for medium and large particles below 3.5 km

395   (10 km). During HALO-(AC)^3, η is similar regardless of size. However, positive η_{IWC}—indicating the occurrence of IWC clusters— are shifted to slightly larger lags for large particles (9 km as opposed to 5-6 km for small and medium sizes).

The measurement location in-cloud could influence the dependency of N_i and IWC variability on particle size due to size sorting, i.e., more small particles near CTH and larger particles at lower height. During the analyzed HALO-(AC)^3 segments, clouds were shallow and *Polar 6* measurements took place on average 440 m below the CTH (as measured by W-band radar).

400   During IMPACTS, much deeper cloud systems were observed and *P-3* sampled on average in larger vertical distances from cloud top (3.3 km) than during HALO-(AC)^3. W-band radar reflectivity Z_e—which can be seen as a proxy for IWC—shows higher variability close to CTH for both IMPACTS and HALO-(AC)^3 clouds (Fig. 8). Similar to Fig. 7, we use PCF to characterize the variability of Z_e in linear units. For each IMPACTS (HALO-(AC)^3) flight segment, η is calculated for Z_e cross sections in 100 m (50 m) steps from the average CTH downward. In general, Z_e variability is larger close to cloud top

405   at lags below 5 km and 2 km for IMPACTS and HALO-(AC)^3, respectively. The higher variability is likely linked to cloud
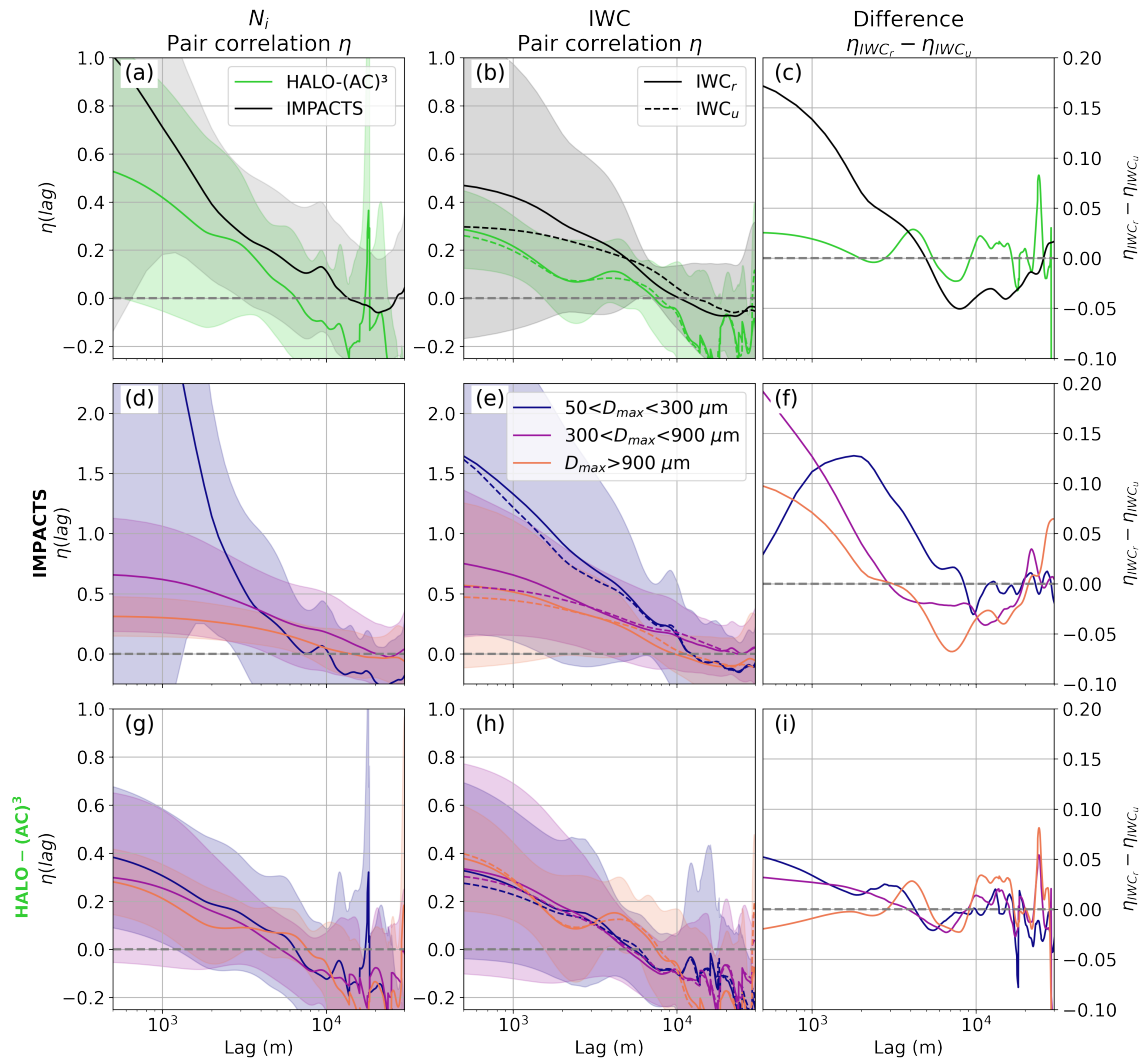
Figure 7. Average pair correlation function (PCF) η as a function of lag calculated for (a) ice number concentration N_i and (b) ice water content (IWC) during IMPACTS (black) and HALO-(AC)^3 (green) segments. IWC is calculated with (solid line) and without (dashed line) accounting for riming and differences are plotted in (c). Shaded areas show standard deviations. In (d)-(i), the particle size distributions are split into small ($50 < D_{max} < 300$ μm), medium ($300 < D_{max} < 900$ μm), and large ($D_{max} > 900$ μm) particle sizes. (d)-(f) and (g)-(i) are as in (a)-(c) but showing size dependency of η during IMPACTS and HALO-(AC)^3, respectively. Note the different y-axis scales.

top generating cells, which can be seen e.g., in case study 1 (Fig. 3a). Generating cells contain more liquid and ice and have stronger updrafts than adjacent cloud regions. HALO-(AC)^3 clouds show less variability and are homogeneous on smaller spatial scales ($\eta = 0$ is at smaller lags) than clouds during IMPACTS. Size sorting might play a larger role for IMPACTS due to the larger cloud depths as opposed to the shallow MCAO clouds during HALO-(AC)^3. However, N_i and IWC distributions as
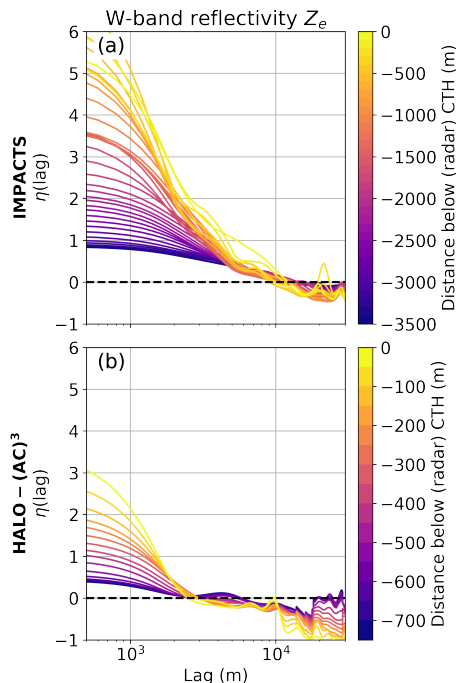
Figure 8. Average pair correlation function (PCF) η as a function of lag calculated for horizontal cross section of W-band Z_e (in linear units) during (a) IMPACTS and (b) HALO-(AC)[3] flight segments. Cross sections are taken in 100 m and 50 m steps from the average cloud top height (CTH) of each segment downward for IMPACTS and HALO-(AC)[3] data, respectively. Note the different colorbar scales.

410   functions of distance to CTH indicate the opposite (Appendix B). Nonetheless, N_i and IWC derived for small particles only show much more variability depending on the distance to CTH for IMPACTS (Appendix B).

The higher variability of small particle counts during IMPACTS is therefore likely due to higher numbers of ice nucleating particles (INP) available at mid-latitudes (Petters and Wright, 2015). During the analyzed HALO-(AC)[3] flight days, INP concentrations collected with filters on board of *Polar 6* were very low, oftentimes below the detection threshold (Wendisch
415   et al., 2024). No INP measurements were conducted during IMPACTS, therefore a direct comparison cannot be made. Another explanation could possibly be more secondary ice production (SIP) occurring during IMPACTS than during HALO-(AC)[3].

Differences between η computed for IWC$_r$ and IWC$_u$ using the different size bins (Fig. 7f) show that riming enhances the probability of IWC clusters for lags smaller 9 km for small particles during IMPACTS. For medium and large particles, riming enhances IWC cluster probability at lags smaller 3 km. The enhancement is larger the smaller the lag for medium
420   and large particles, whereas for small particles the largest enhancement is at a lag of about 2 km. An enhancement for small particles possibly hints at SIP connected to riming such as rime splintering. During HALO-(AC)[3] (Fig. 7i), riming enhances the probability of IWC clusters for lags smaller 4 km for small and medium particles and the enhancement is generally larger the smaller the lag. For large particles only lags of about 3-5 km lead to an enhancement of IWC variability.
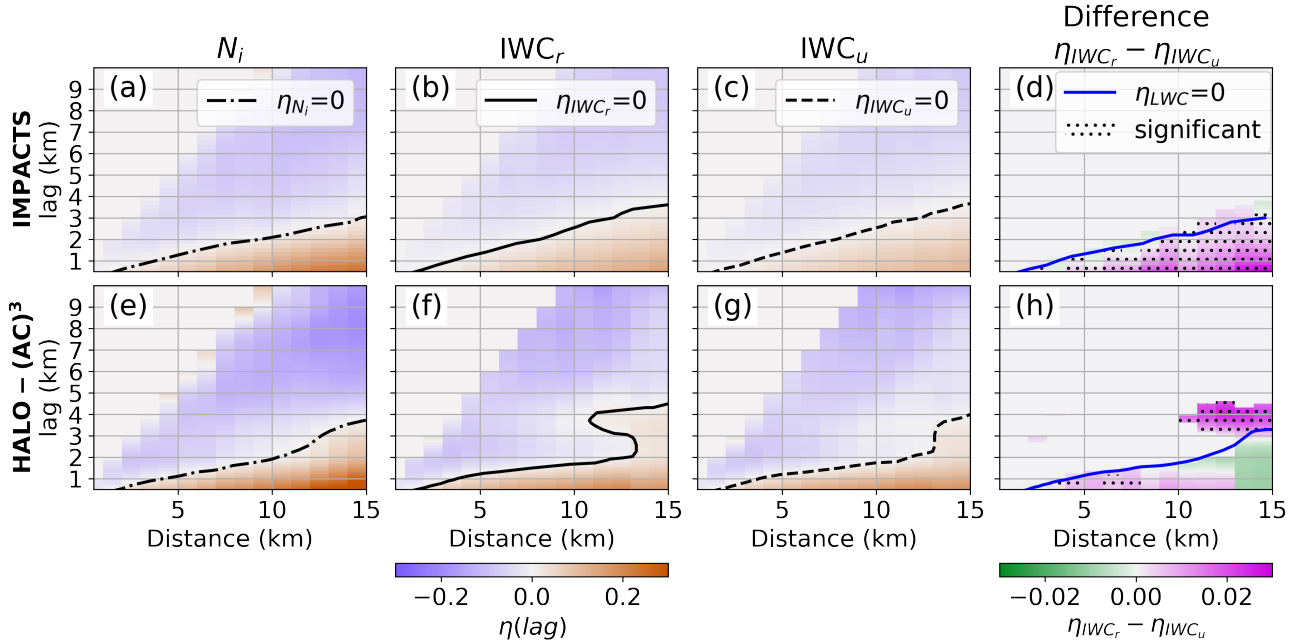
Figure 9. Average pair correlation function (PCF) η as a function of distance and lag calculated using all (a-c) IMPACTS and (e-g) HALO-$(AC)^3$ flight segments for (a)&(e) N_i, (b)&(f) ice water content (IWC) accounting for riming IWC_r, and (c)&(g) IWC assuming no riming IWC_u. The Difference between (b) and (c) are shown in (d); difference between (f) and (g) in (h). Differences in (d) and (h) are only shown, where $\eta_{IWC_r} > 0$. Areas, where differences are significant according to a Student's t-test (95 % significance threshold) are hatched. $\eta = 0$ is drawn as shaded lines for the ice number concentration N_i (dash-dotted black), IWC_r (solid black), IWC_u (dashed black), and liquid water content (LWC, solid blue), where LWC measurements from King probe (Nevzorov probe) measurements obtained during IMPACTS (HALO-$(AC)^3$) are used.

4.3.2 Dependency on riming

425 To understand which spatial scales dominate the riming driven IWC variability, we conduct a Monte-Carlo random test for specific sampling distances following Deng et al. (2024). This approach allows us to first, handle the flight segments of different lengths in a statistically robust way, and second, analyze the dependence on flight segment distance. For each flight segment, we randomly select a sub-segment with a distance of d km, where we vary d in 1 km steps from 1 to 15 km. Then, we calculate η for this segment. This is repeated 100 times and the average η over all (sub)segments of the respective campaign is 430 calculated. To perform the averaging, we bin η into 200 m and 60 m bins for IMPACTS and HALO-$(AC)^3$, respectively, which corresponds to the respective distances covered in 1 s for the respective typical flight speeds. The results are shown in Fig. 9, where the average η for N_i, IWC_r, and IWC_u are plotted as functions of distance d and lag. Curves (shaded) where $\eta = 0$ are included to show the maximum spatial scales at which ice clusters likely occur, given a sampling distance d.

During IMPACTS, the maximum N_i cluster spatial scale in clouds increases from 0.6 km to 3.1 km at distances d of 2 km to 15 km (Fig. 9a). King probe-measured LWC cluster scales behave similarly to N_i (not shown) and maximum cluster scales increase from 0.6 km to 3.0 km. This suggests simultaneous liquid and ice formation in regions with high supersaturation with respect to ice. Maximum IWC cluster scales (independent of accounting for riming or not) increase from 0.6 km to 3.6 km (Fig. 9b,c). At distances smaller 6 km, N_i and IWC have about the same cluster scales; at distances larger 10 km, IWC clusters occur at larger spatial scales. Differences between positive values of IWC$_r$ and IWC$_u$ (Fig. 9d) reveal that riming enhances the probability of ice clusters for distances larger 6 km for lags from about 1 km to 10 km (at distances of 12 km). To show the statistical significance of this enhancement, a one-sided Student's t-test with a significance threshold of 95 % is used. Areas where differences are significant are hatched (Fig. 9d). The enhancement occurs at similar spatial scales as LWC clusters, indicating riming is driven by LWC variability.

During HALO-(AC)[3], the maximum N_i cluster spatial scale in clouds increases from 0.5 km to 3.7 km at distances of 2 km to 15 km (Fig. 9e). Similar to IMPACTS data, Nevzorov probe measured LWC clusters behave similarly, increasing from 0.5 km to 3.3 km, however having slightly smaller spatial scales. Maximum IWC cluster scales assuming no riming increase from 0.6 km to 3.8 km and therefore occur at about the same spatial scales as N_i clusters (Fig. 9g). When accounting for riming, maximum IWC cluster scales show a distinct behavior for distances larger 10 km: η increases at 3-5 km indicating that riming enhances variability on these scales (Fig. 9f), which cannot be explained by the LWC variability. Statistically significant differences between positive IWC$_r$ and IWC$_u$ (Fig. 9h), further highlight this feature.

To explain the different spatial scales where riming enhances IWC variability, we look at lidar derived CTH. In previous sections, we derived CTH from radar measurements to make IMPACTS and HALO-(AC)[3] comparable. During HALO-(AC)[3] a more sophisticated CTH product based on lidar—which is more sensitive to liquid layers at cloud top than the radar—is available and used the following. The lidar detects small liquid droplets at cloud top, which follow vertical motions, therefore leading to higher CTH in updraft regions (Abel et al., 2017). When computing the average power spectrum of CTH observed during the studied flight days, distinct peaks at wavelengths of 750 m and 1.2 km occur for all days, which corresponds to the typical roll cloud and circulation wavelengths as derived by Schirmacher, et al. (2024) (Fig. 10a, d, g). At these wavelengths, peaks in LWP also occur for all days (Fig. 10b, e, h) further indicating enhanced formation and growth of liquid droplets in the updraft regions of the convectional cell cloud structures. On 28 March, a distinctive peak in the CTH spectrum at 3-5 km indicates additional mesoscale updraft features (Fig. 10a). However, the LWP spectrum only shows a weak peak towards 5 km (Fig. 10b). On 1 April, both CTH and LWP power spectra have peaks at 3-5 km (Fig. 10d,e). On 4 April, no peak distinctive peaks at wavelengths of 3-5 km are visible (Fig. 10g,h). Given that the least (most) amount of riming (Fig. 10c,f,i) occurred on 4 (1) April, we conclude that in the studied MCAO clouds mesoscale updraft features likely enhance riming at spatial scales of 3-5 km. The enhancement could occur either due to prolonged lifetimes of ice crystals in clouds (28 March) or increased amounts of liquid water or both (01 April) and leads to an increase in IWC amount and variability.
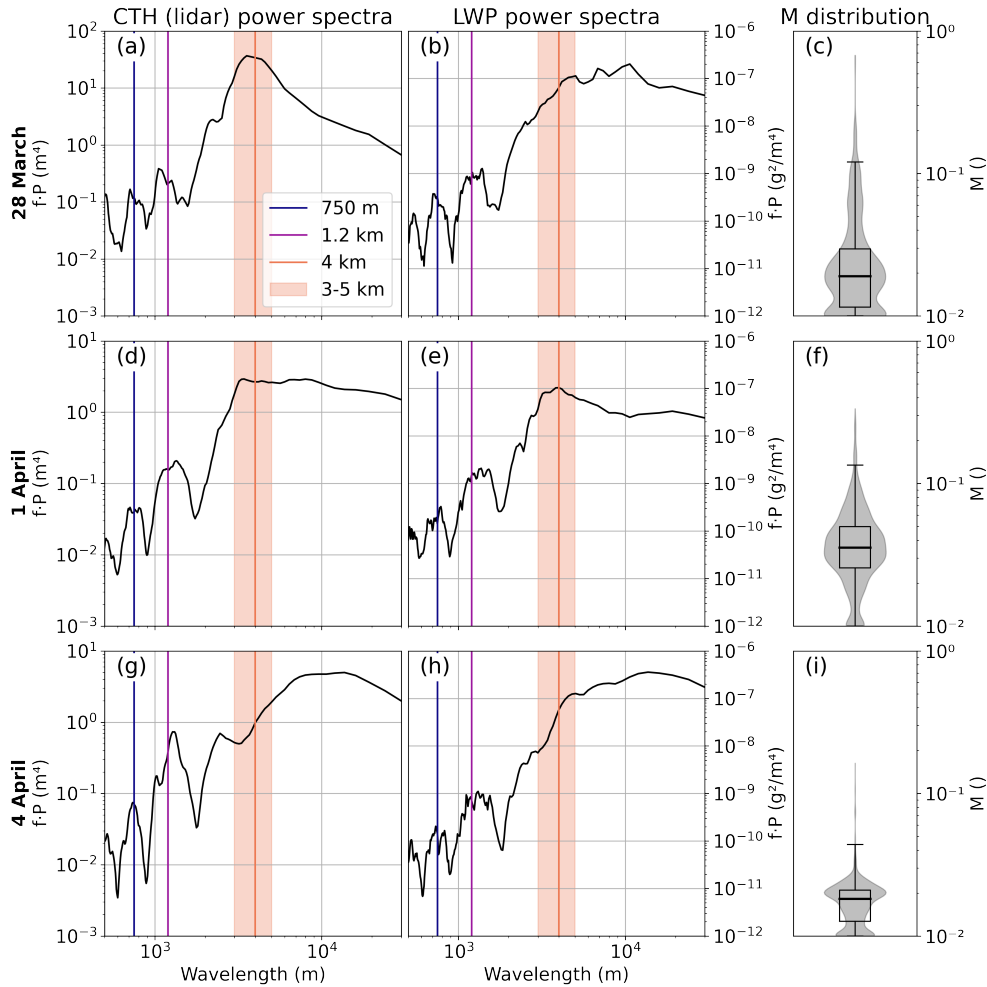
Figure 10. Power spectra of (a), (d), and (g) cloud top height (CTH) as derived from lidar and (b), (e), and (h) liquid water path (LWP) during collocated HALO-(AC)^3 flight days. The wavelength has been calculated based on the aircraft flight speed. The blue and purple lines show the typical roll cloud and circulation wavelengths as derived by Schirmacher, et al. (2024). The orange shaded area shows the 3-5 km range, where riming causes additional IWC clustering. (c), (f), and (i) show the corresponding normalized rime mass M distributions.

4.4 A conceptual model of how riming impacts IWC clusters in MCAO roll clouds

The results discussed above help to better understand scales of in-cloud IWC clustering in different types of MPC and link to some microphysical processes involved. Although there are substantial unknowns, the following summarizes our findings from the perspective of collocated remote sensing and in situ measurements.

470   In the analyzed segments of winter storm clouds measured during IMPACTS, IWC clusters occur at spatial scales smaller than about 3 km for segment distances of 15 km. Accounting for riming enhances ice cluster probabilities (Fig. 9d). However, riming does not lead to significantly enhanced occurrences of IWC clusters at other scales. LWC clusters for segment distances

23
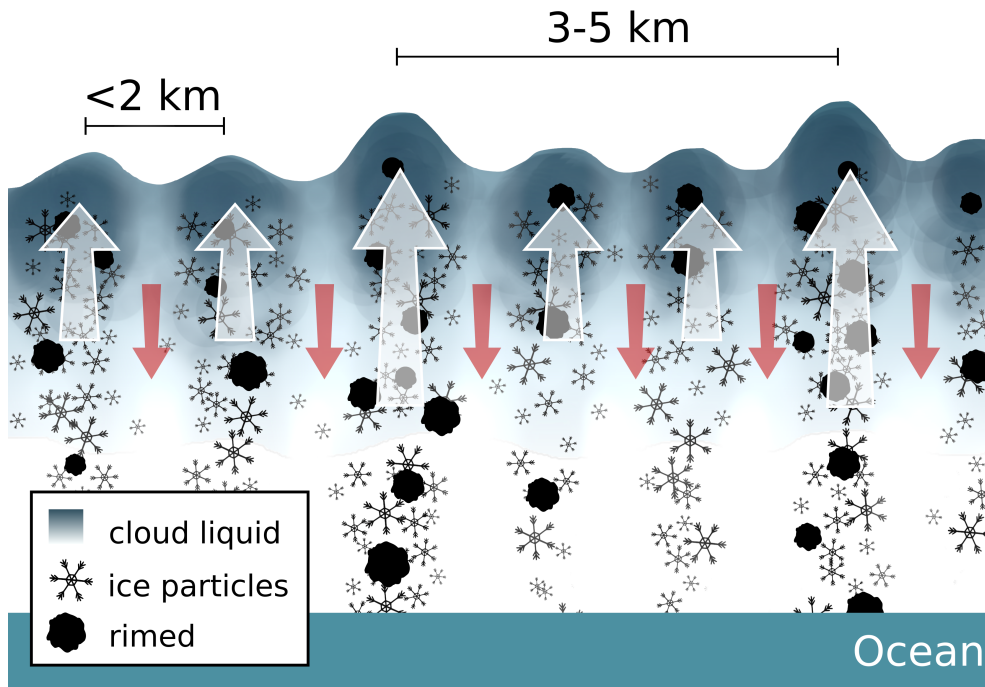
Figure 11. A conceptual diagram summarizing ice cluster spatial scales driven by riming as observed in MCAO roll clouds during HALO-(AC)[3]. For further explanations see text.

of 15 km occur at the same spatial scales of about 3 km as clusters of N_i. Therefore, liquid droplets and ice particles are likely formed together in regions with supersaturation with respect to liquid and ice. Because LWC clusters and the IWC

475   cluster enhancement through riming occur at similar spatial scales, we hypothesize that LWC variability (at least in part) drives riming. By increasing IWC, riming leads to enhanced probabilities of IWC clusters for IMPACTS.

For HALO-(AC)[3], Fig. 11 shows a sketch of the maximum spatial scales, where we found ice clusters to occur for MPCs observed during MCAOs. In these MCAO roll clouds, ice clusters occur at spatial scales of the roll cloud wavelengths. In the updraft regions of the convectional cells, which occurred on average every 750 m and 1.2 km, liquid droplets and ice particles

480   are formed. LWP and CTH are increased due to the vertical motions and liquid condensation. Ice particles grow through depositional growth and riming, which leads to enhanced probabilities of ice clusters at these scales. When ice particles' masses have increased sufficiently, they precipitate or might sublimate below cloud. Aggregation might occur as ice particles collide. In the presence of additional mesoscale updraft features, IWC clusters also occur at spatial scales of 3-5 km (Fig. 9h). Due to the stronger vertical motion, ice particles are suspended longer, have more time to rime and can reach higher

485   masses before precipitating. Increased LWP might enhance the amount of riming, but is not a necessary criterion based on the analyzed cases. This hypothesis is supported by the fact that the observed LWP is not sufficient to explain the retrieved rime masses assuming particles continuously collecting liquid water by falling through the liquid layer as we show in Appendix C. The enhanced occurrence of riming drives the additional increase of IWC cluster probability at spatial scales of 3-5 km.

5 Conclusions

In this study, airborne measurements of mixed-phase clouds (MPC) in mid- and high-latitudes are used to study spatial variability of ice clusters within clouds. We further investigate how this variability is linked to riming, which we quantify by closure of collocated cloud radar reflectivity and in situ particle size distribution (PSD) measurements. Pair correlation function (PCF) is used to quantify ice cluster scales and ice water content (IWC) variability when first, accounting for riming (IWC_r), and second, neglecting riming (IWC_u). The main findings are as follows:

1. Although synoptic situations and the resulting clouds systems were vastly different during the two analyzed aircraft campaigns, the retrieved amounts of riming were similar with median normalized rime masses M of 0.023 and 0.024 during IMPACTS (mid-latitude winter storms) and HALO-(AC)^3 (Arctic MCAO roll clouds) segments, respectively (Fig. 5). Clouds were deep (shallow) during IMPACTS (HALO-(AC)^3) segments and in situ measurements were conducted on average in vertical distances of 3.3 km (440 m) from cloud top.

2. The observed spread of M can increase IWC up to two orders of magnitude, depending on the size of the particle population (Fig. 6). In sum, rime mass makes up about 66 % and 63 % of total IWC during the analyzed IMPACTS and HALO-(AC)^3 flight segments, respectively. Therefore, riming has a similar impact on IWC as the observed spread of number concentration and should not be neglected when estimating IWC.

3. PCF revealed that N_i cluster occur with increased probability on spatial scales smaller 10.5 km and 6.5 km within clouds during IMPACTS and HALO-(AC)^3, respectively. IWC clusters dominate for spatial scales of 10 km and 7 km. During IMPACTS, small particles dominate N_i and IWC variability on small spatial scales, whereas there is no dependence on particle size during HALO-(AC)^3 (Fig. 7). This could be linked to ice formation processes and the higher availability of INP at mid-latitudes. However, this hypothesis could not be confirmed with the available data.

4. During IMPACTS, maximum N_i, IWC and LWC cluster spatial scales inside clouds are 0.6 km for distances of 2 km and increase to about 3 km for distances of 15 km. During HALO-(AC)^3, maximum N_i, IWC and LWC cluster spatial scales are similar with about 0.5 km for distances of 2 km and about 4 km for 15 km. However, during HALO-(AC)^3 IWC cluster probability is increased on scales of 3-5 km when segment distances are larger 10 km (Fig. 9).

5. During IMPACTS, accounting for riming does not significantly change IWC cluster scales in clouds, but increases the probability of clusters for segment distances larger than 6 km (Fig. 9d). This enhancement occurs at similar scales as LWC variability. More riming likely occurs in regions with enhanced concentration of liquid water and increases IWC. Since clusters of IWC neglecting riming have similar spatial scales as N_i, LWC, and IWC accounting for riming, ice clustering is likely linked to ice formation processes in regions of high supersaturation with respect to liquid and ice .

6. In contrast, riming impacts IWC clustering in clouds at two distinctive scales during HALO-(AC)^3 (Fig. 9h). First, riming enhances the probability of IWC clusters at spatial scales below 2 km, which corresponds to the wavelength of the roll cloud updraft features. N_i, IWC_r, IWC_u, and LWC all have similar spatial variability indicating simultaneous

ice and liquid formation and growth in this regions. The enhanced concentrations of liquid again enhance riming, which increases IWC. Second, riming leads to IWC clustering at spatial scales of 3-5 km, which cannot be explained by the typical roll cloud and roll circulation wavelengths. Power spectra of CTH show peaks at these spatial scales on the flight days with enhanced riming (Fig. 10). This indicates that the presence of mesoscale updraft features—which cause higher lifting of small particles near cloud top and therefore increased CTH—leads to enhanced occurrence of riming and therefore additional IWC clustering. Increased LWP might increase the effect, but is not a necessary criterion based on the analyzed days. Theoretical analysis shows that updrafts are likely required to explain the observed riming values (Fig. C1).

These results help to improve our understanding of how riming is linked to in-cloud IWC variability and can be used to evaluate and constrain MPC models. While we have shown that riming enhances in-cloud IWC variability and causes additional IWC clustering at large spatial scales of 3-5 km in Arctic MCAO clouds, further research is needed to link these findings to surface precipitation. Future studies should investigate the link between riming-driven IWC variability and snowfall variability. In addition, profiles of vertical wind speed and turbulence are needed to better understand their importance for riming.

Appendix A: Microphysical overview of analyzed segments

Figure A1 (A2) presents an overview of microphysical parameters (N_i, D_{32}, M, IWC, LWC) observed during each analyzed IMPACTS (HALO-(AC)[3]) segment. Case study 1 (case study 2) is the fifth segment on 5 February (second segment on 1 April).
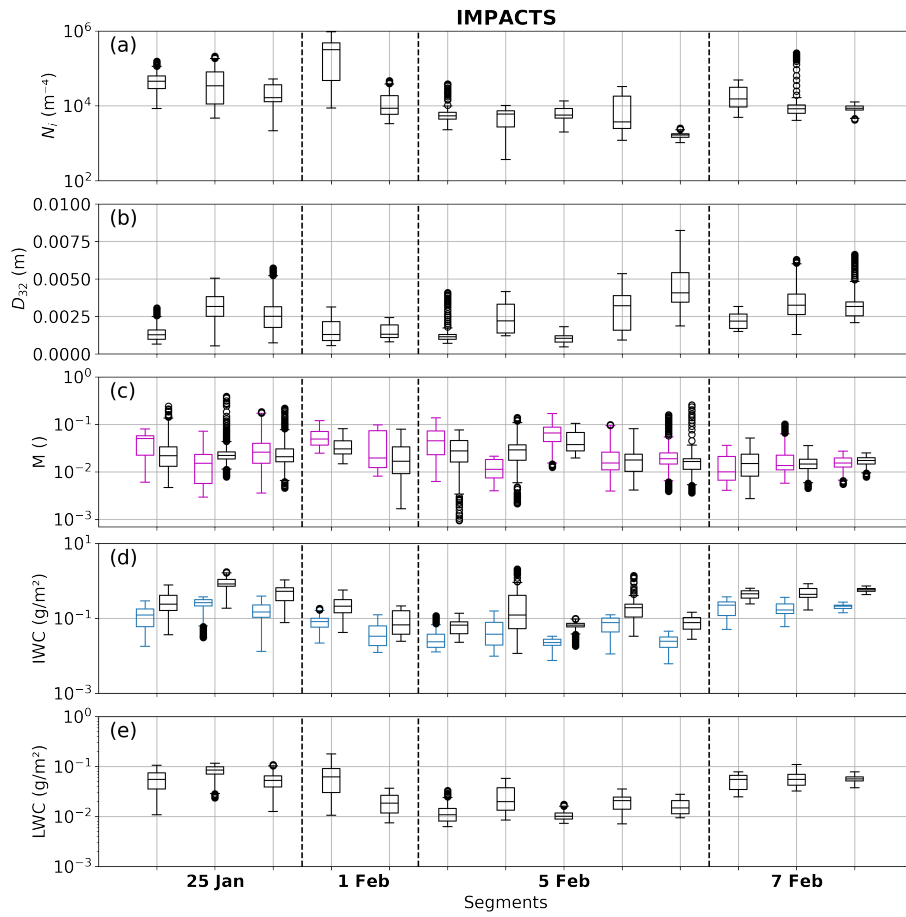
Figure A1. Boxplots of (a) ice number concentration N_i, (b) mass-weighted diameter D_{32}, (c) normalized rime mass M, (d) ice water content (IWC), and (e) liquid water content (LWC) derived during each IMPACTS segment. In (c) both combined (Ku-band) and in situ method results are shown in black and magenta, respectively. In (d) IWC is calculated accounting for riming (using combined method M; black) and neglecting riming ($M = 0$, blue).
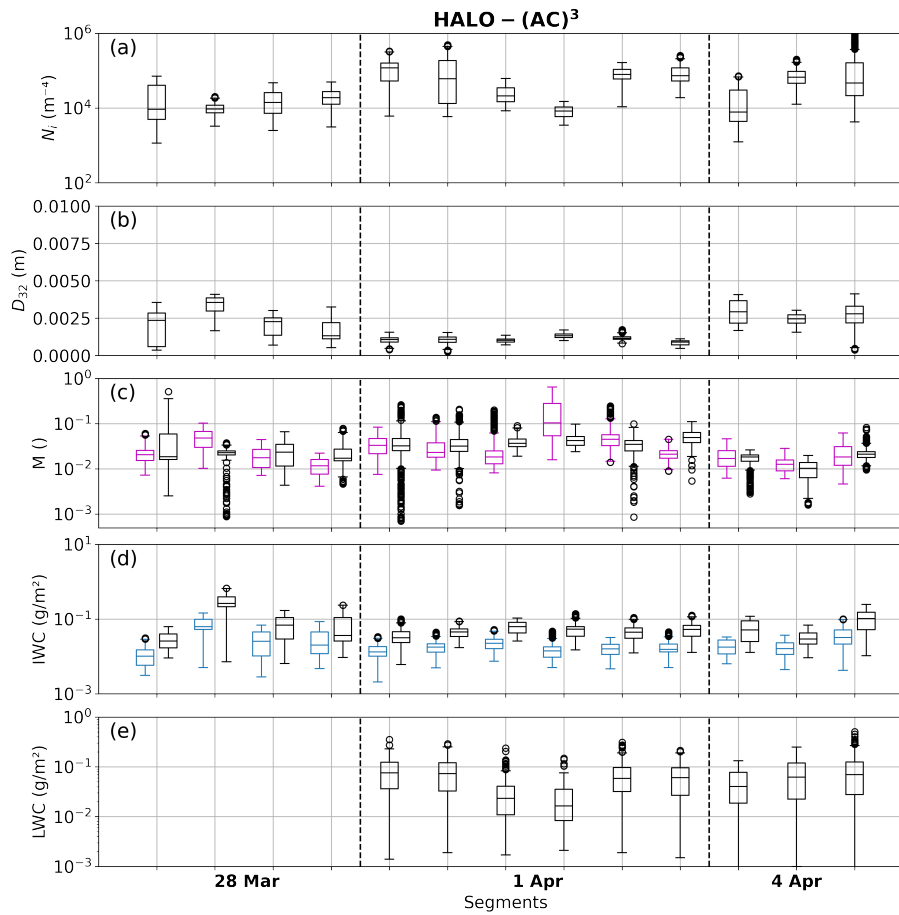
Figure A2. As in Fig. A1 but for HALO-(AC)^3 segments

Appendix B: Vertical distribution of N_i and IWC

To investigate whether size sorting is the reason of the particle size dependency of N_i and IWC variability (Sect. 4.3.1), we show vertical distributions of N_i and IWC for the different size ranges in Fig. B1 and Fig. B2, respectively. Data during collocated segments is binned by their distance to CTH (as derived by radar measurements) in 100 m bins. Only bins with minimum 100 data points are shown. This leaves no data for 1.5 km below cloud top during IMPACTS. While HALO-(AC)^3 data shows size sorting close to cloud top for both N_i and IWC, this is not the case for IMPACTS. However, size sorting could have happened in the vertical region where we lack data. Nonetheless, N_i and IWC for small particles show much larger variability during IMPACTS than during HALO-(AC)^3 regardless of distance to cloud top.
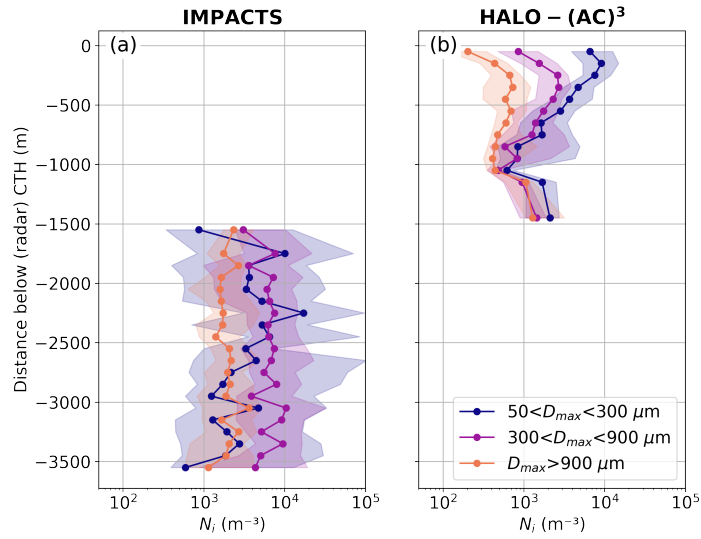
Figure B1. Distribution of ice number concentration N_i as a function of distance to cloud top height (CTH, derived by radar) for (a) IMPACTS and (b) HALO-(AC)[3]. Lines and markers show median values; 25-75 % quantiles are shaded. Contributions of small (50-300 μm), medium (300-900 μm), and large (>900 μm) particles are shown in blue, purple, and orange.
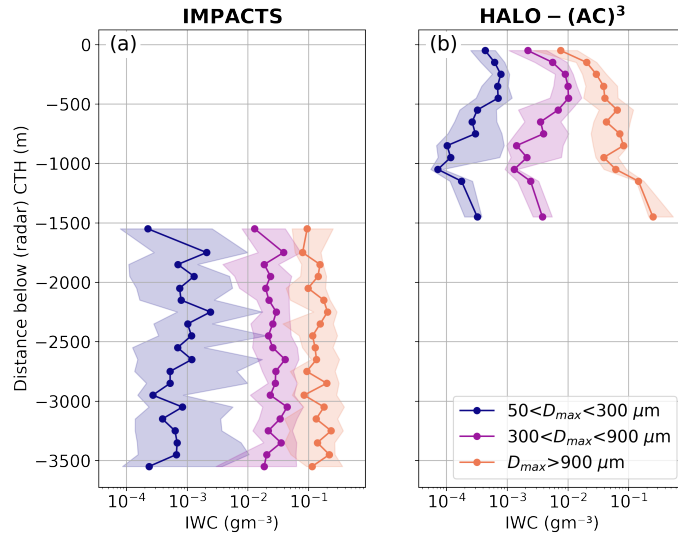
Figure B2. As in Fig. B1 but for ice water concent (IWC; calculated accounting for riming).

Appendix C: LWP riming calculations

555   This section shows the need for updrafts to explain the retrieved amounts of riming given the observed LWPs. We use simple calculations based on Fitch and Garrett (2022). Assuming a particle collects rime by falling through a liquid layer, the mass of rime accumulated can be approximated by

$$m_{rime} = A_p \, E_c \, \text{LWP}, \qquad\qquad\qquad\qquad (C1)$$

where A_p is the cross-sectional area of the particle, E_c the combined collection and collision efficiency, and LWP the liquid
560   water path of the liquid layer. By inserting the definition of M, approximating A_p by a power law function of $D_{\max}$ with prefactor a_A and exponent b_A following Maherndl et al. (2023a), and solving for LWP, we derive

$$\text{LWP} = \frac{M \, m_g}{A_p} = \frac{\pi \, \rho_g \, M}{6 \, a_A(M)} \, D_{max}^{3-b_A(M)}. \qquad\qquad\qquad (C2)$$

Here, E_c is assumed to be 1 as a worst case estimate, although in the Arctic lower values are more realistic (Fitch and Garrett, 2022). Eq. C2 only holds for ice particles that have finished the riming process. It is therefore only applied to HALO-(AC)[3]
565   data, where LWC= 0 was measured, thereby we exclude 28 March data, where LWC measurements are not available. Because ice particles occur in PSDs, we apply Eq. C2 to D_{32} as a proxy for the characteristic size and the respective M we retrieved for each time step. Compared to LWP observations during 1 and 4 April, the calculated LWP is much higher (Fig. C1). Therefore, it is evident, that the particles must have been exposed to the liquid layer multiple times, e.g., by cycling through up- and downdraft regions.
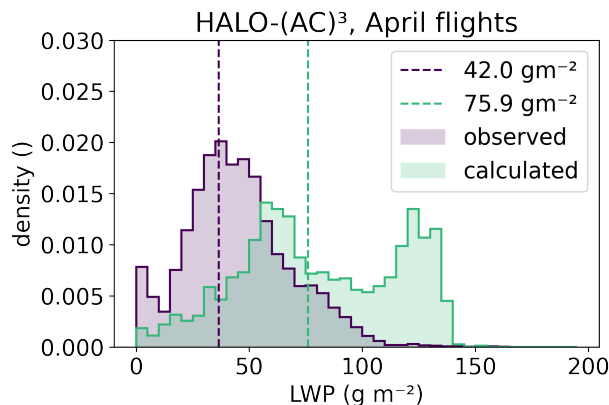

Figure C1. Normalized histograms of observed and calculated liquid water path (LWP) including medians (dashed lines). Observed LWP are from all 1 and 4 April data points. Calculated LWP were only derived for time steps where LWC= 0, such that it can be assumed that no further riming will take place.

References

590 NASA Worldview, MODIS level-2 cloud product, https://worldview.earthdata.nasa.gov.

Abel, S. J., Boutle, I. A., Waite, K., Fox, S., Brown, P. R. A., Cotton, R., Lloyd, G., Choularton, T. W., and Bower, K. N.: The Role of Precipitation in Controlling the Transition from Stratocumulus to Cumulus Clouds in a Northern Hemisphere Cold-Air Outbreak, Journal of the Atmospheric Sciences, 74, 2293 – 2314, https://doi.org/10.1175/JAS-D-16-0362.1, https://journals.ametsoc.org/view/journals/atsc/74/7/jas-d-16-0362.1.xml, 2017.

595 Baker, B. and Lawson, R. P.: Analysis of Tools Used to Quantify Droplet Clustering in Clouds, Journal of the Atmospheric Sciences, 67, 3355–3367, ISSN 0022-4928, 1520-0469, https://doi.org/10.1175/2010JAS3409.1, 2010.

Bansemer, A., Delene, D., Heymsfield, A. J., O'Brien, J., Poellot, M. R., Sand, K., Sova, G., Moore, J., and Nairy, C.: NCAR Particle Probes IMPACTS.Dataset available online from the NASA Global Hydrometeorology Resource Center DAAC, Huntsville, Alabama, U.S.A. , https://doi.org/10.5067/IMPACTS/PROBES/DATA101, http://dx.doi.org/10.5067/IMPACTS/PROBES/DATA101, 2022.

600 Baumgardner, D., Jonsson, H., Dawson, W., O'Connor, D., and Newton, R.: The Cloud, Aerosol and Precipitation Spectrometer: A New Instrument for Cloud Investigations, Atmospheric Research, 59–60, 251–264, ISSN 0169-8095, https://doi.org/10.1016/S0169-8095(01)00119-3, 2001.

Baumgardner, D., Abel, S. J., Axisa, D., Cotton, R., Crosier, J., Field, P., Gurganus, C., Heymsfield, A., Korolev, A., Krämer, M., Lawson, P., McFarquhar, G., Ulanowski, Z., and Um, J.: Cloud Ice Properties: In Situ Measurement Challenges, Meteorological Monographs, 58, 605 9.1–9.23, https://doi.org/10.1175/AMSMONOGRAPHS-D-16-0011.1, 2017.

Bjordal, J., Storelvmo, T., Alterskjær, K., and Carlsen, T.: Equilibrium Climate Sensitivity above 5 °C Plausible Due to State-Dependent Cloud Feedback, Nature Geoscience, 13, 718–721, ISSN 1752-0908, https://doi.org/10.1038/s41561-020-00649-1, 2020.

Bock, J., Michou, M., Nabat, P., Abe, M., Mulcahy, J. P., Olivié, D. J. L., Schwinger, J., Suntharalingam, P., Tjiputra, J., van Hulten, M., Watanabe, M., Yool, A., and Séférian, R.: Evaluation of Ocean Dimethylsulfide Concentration and Emission in CMIP6 Models, 610 Biogeosciences, 18, 3823–3860, ISSN 1726-4170, https://doi.org/10.5194/bg-18-3823-2021, 2021.

Cao, Q., Huang, Y., Zou, J., Lin, W., Zhou, X., Li, H., and Zhang, X.: Predicted Particle Properties (P3) Microphysics Scheme Coupled With WRF-Chem Model: Evaluation With Convective and Stratiform Cases, Journal of Geophysical Research: Atmospheres, 128, e2022JD037 685, https://doi.org/https://doi.org/10.1029/2022JD037685, https://agupubs.onlinelibrary.wiley.com/doi/abs/10.1029/2022JD037685, e2022JD037685 2022JD037685, 2023.

615 Chase, R. J., Finlon, J. A., Borque, P., McFarquhar, G. M., Nesbitt, S. W., Tanelli, S., Sy, O. O., Durden, S. L., and Poellot, M. R.: Evaluation of Triple-Frequency Radar Retrieval of Snowfall Properties Using Coincident Airborne In Situ Observations During OLYMPEX, Geophysical Research Letters, 45, 5752–5760, ISSN 1944-8007, https://doi.org/10.1029/2018GL077997, https://onlinelibrary.wiley.com/doi/abs/10.1029/2018GL077997, 2018.

Choi, Y.-S., Ho, C.-H., Park, C.-E., Storelvmo, T., and Tan, I.: Influence of Cloud Phase Composition on Climate Feedbacks, Journal of 620 Geophysical Research: Atmospheres, 119, 3687–3700, ISSN 2169-8996, https://doi.org/10.1002/2013JD020582, 2014.

Connelly, R. and Colle, B. A.: Validation of Snow Multibands in the Comma Head of an Extratropical Cyclone Using a 40-Member Ensemble, Weather and Forecasting, 34, 1343–1363, ISSN 1520-0434, 0882-8156, https://doi.org/10.1175/WAF-D-18-0182.1, 2019.

Delanoë, J., Protat, A., Testud, J., Bouniol, D., Heymsfield, A. J., Bansemer, A., Brown, P. R. A., and Forbes, R. M.: Statistical Properties of the Normalized Ice Particle Size Distribution, Journal of Geophysical Research: Atmospheres, 110, ISSN 2156-2202, 625 https://doi.org/10.1029/2004JD005405, 2005.

Delanoë, J. M. E., Heymsfield, A. J., Protat, A., Bansemer, A., and Hogan, R. J.: Normalized Particle Size Distribution for Remote Sensing Application, Journal of Geophysical Research: Atmospheres, 119, 4204–4227, ISSN 2169-8996, https://doi.org/10.1002/2013JD020700, 2014.

Deng, Y., Yang, J., Yin, Y., Cui, S., Zhang, B., Bao, X., Chen, B., Li, J., Gao, W., and Jing, X.: Quantifying the Spatial Inhomogeneity of Ice Concentration in Mixed-Phase Stratiform Cloud Using Airborne Observation, Atmospheric Research, 298, 107 153, ISSN 0169-8095, https://doi.org/10.1016/j.atmosres.2023.107153, 2024.

Erfani, E. and Mitchell, D. L.: Growth of Ice Particle Mass and Projected Area during Riming, Atmospheric Chemistry and Physics, 17, 1241–1257, ISSN 1680-7316, https://doi.org/10.5194/acp-17-1241-2017, 2017.

Field, P. R., Hogan, R. J., Brown, P. R. A., Illingworth, A. J., Choularton, T. W., Kaye, P. H., Hirst, E., and Greenaway, R.: Simultaneous Radar and Aircraft Observations of Mixed-Phase Cloud at the 100 m Scale, Quarterly Journal of the Royal Meteorological Society, 130, 1877–1904, ISSN 1477-870X, https://doi.org/10.1256/qj.03.102, 2004.

Finlon, J. A., McMurdie, L. A., and Chase, R. J.: Investigation of Microphysical Properties within Regions of Enhanced Dual-Frequency Ratio during the IMPACTS Field Campaign, Journal of the Atmospheric Sciences, 79, 2773–2795, ISSN 0022-4928, 1520-0469, https://doi.org/10.1175/JAS-D-21-0311.1, 2022.

Fitch, K. E. and Garrett, T. J.: Graupel Precipitating From Thin Arctic Clouds With Liquid Water Paths Less Than 50 g M-2, Geophysical Research Letters, 49, e2021GL094 075, ISSN 1944-8007, https://doi.org/10.1029/2021GL094075, 2022.

Harimaya, T. and Sato, M.: Measurement of the Riming Amount on Snowflakes, Journal of the Faculty of Science, Hokkaido University, 8, 355–366, 1989.

Heymsfield, A. J.: A Comparative Study of the Rates of Development of Potential Graupel and Hail Embryos in High Plains Storms, Journal of the Atmospheric Sciences, 39, 2867–2897, ISSN 0022-4928, 1520-0469, https://doi.org/10.1175/1520-0469(1982)039<2867:ACSOTR>2.0.CO;2, 1982.

Heymsfield, A. J., Schmitt, C., Bansemer, A., and Twohy, C. H.: Improved Representation of Ice Particle Masses Based on Observations in Natural Clouds, Journal of the Atmospheric Sciences, 67, 3303–3318, ISSN 0022-4928, 1520-0469, https://doi.org/10.1175/2010JAS3507.1, 2010.

Heymsfield, G. M., Bidwell, S. W., Caylor, I. J., Ameen, S., Nicholson, S., Boncyk, W., Miller, L., Vandemark, D., Racette, P. E., and Dod, L. R.: The EDOP Radar System on the High-Altitude NASA ER-2 Aircraft, Journal of Atmospheric and Oceanic Technology, 13, 795–809, ISSN 0739-0572, 1520-0426, https://doi.org/10.1175/1520-0426(1996)013<0795:TERSOT>2.0.CO;2, 1996.

Heymsfield, G. M., Li, L., and McLinden, M.: ER-2 X-Band Doppler Radar (EXRAD) IMPACTS. Dataset available online from the NASA Global Hydrometeorology Resource Center DAAC, Huntsville, Alabama, U.S.A. , https://doi.org/10.5067/IMPACTS/EXRAD/DATA101, http://dx.doi.org/10.5067/IMPACTS/EXRAD/DATA101, 2022.

Houze, R. A., McMurdie, L. A., Petersen, W. A., Schwaller, M. R., Baccus, W., Lundquist, J. D., Mass, C. F., Nijssen, B., Rutledge, S. A., Hudak, D. R., Tanelli, S., Mace, G. G., Poellot, M. R., Lettenmaier, D. P., Zagrodnik, J. P., Rowe, A. K., DeHart, J. C., Madaus, L. E., Barnes, H. C., and Chandrasekar, V.: The Olympic Mountains Experiment (OLYMPEX), Bulletin of the American Meteorological Society, 98, 2167–2188, ISSN 0003-0007, 1520-0477, https://doi.org/10.1175/BAMS-D-16-0182.1, 2017.

King, W. D., Parkin, D. A., and Handsworth, R. J.: A Hot-Wire Liquid Water Device Having Fully Calculable Response Characteristics, Journal of Applied Meteorology and Climatology, 17, 1809–1813, ISSN 1520-0450, https://doi.org/10.1175/1520-0450(1978)017<1809:AHWLWD>2.0.CO;2, 1978.

Kirschler, S., Voigt, C., Anderson, B. E., Chen, G., Crosbie, E. C., Ferrare, R. A., Hahn, V., Hair, J. W., Kaufmann, S., Moore, R. H., Painemal, D., Robinson, C. E., Sanchez, K. J., Scarino, A. J., Shingler, T. J., Shook, M. A., Thornhill, K. L., Winstead, E. L., Ziemba, L. D., and Sorooshian, A.: Overview and Statistical Analysis of Boundary Layer Clouds and Precipitation over the Western North Atlantic Ocean, Atmospheric Chemistry and Physics, 23, 10 731–10 750, ISSN 1680-7316, https://doi.org/10.5194/acp-23-10731-2023, 2023.

Kneifel, S. and Moisseev, D.: Long-Term Statistics of Riming in Nonconvective Clouds Derived from Ground-Based Doppler Cloud Radar Observations, Journal of the Atmospheric Sciences, 77, 3495–3508, ISSN 0022-4928, 1520-0469, https://doi.org/10.1175/JAS-D-20-0007.1, 2020.

Korolev, A. and Milbrandt, J.: How Are Mixed-Phase Clouds Mixed?, Geophysical Research Letters, 49, e2022GL099 578, ISSN 1944-8007, https://doi.org/10.1029/2022GL099578, 2022.

Korolev, A., Emery, E., and Creelman, K.: Modification and Tests of Particle Probe Tips to Mitigate Effects of Ice Shattering, Journal of Atmospheric and Oceanic Technology, 30, 690–708, ISSN 0739-0572, 1520-0426, https://doi.org/10.1175/JTECH-D-12-00142.1, 2013.

Korolev, A., McFarquhar, G., Field, P. R., Franklin, C., Lawson, P., Wang, Z., Williams, E., Abel, S. J., Axisa, D., Borrmann, S., Crosier, J., Fugal, J., Krämer, M., Lohmann, U., Schlenczek, O., Schnaiter, M., and Wendisch, M.: Mixed-Phase Clouds: Progress and Challenges, Meteorological Monographs, 58, 5.1–5.50, https://doi.org/10.1175/AMSMONOGRAPHS-D-17-0001.1, 2017.

Korolev, A. V., Strapp, J. W., Isaac, G. A., and Nevzorov, A. N.: The Nevzorov Airborne Hot-Wire LWC–TWC Probe: Principle of Operation and Performance Characteristics, Journal of Atmospheric and Oceanic Technology, 15, 1495–1510, ISSN 0739-0572, 1520-0426, https://doi.org/10.1175/1520-0426(1998)015<1495:TNAHWL>2.0.CO;2, 1998.

Korolev, A. V., Isaac, G. A., Cober, S. G., Strapp, J. W., and Hallett, J.: Microphysical Characterization of Mixed-Phase Clouds, Quarterly Journal of the Royal Meteorological Society, 129, 39–65, ISSN 1477-870X, https://doi.org/10.1256/qj.01.204, 2003.

Kostinski, A. B. and Jameson, A. R.: On the Spatial Distribution of Cloud Particles, Journal of the Atmospheric Sciences, 57, 901–915, ISSN 0022-4928, 1520-0469, https://doi.org/10.1175/1520-0469(2000)057<0901:OTSDOC>2.0.CO;2, 2000.

Kostinski, A. B. and Shaw, R. A.: Scale-Dependent Droplet Clustering in Turbulent Clouds, Journal of Fluid Mechanics, 434, 389–398, ISSN 1469-7645, 0022-1120, https://doi.org/10.1017/S0022112001004001, 2001.

Lance, S., Brock, C. A., Rogers, D., and Gordon, J. A.: Water Droplet Calibration of the Cloud Droplet Probe (CDP) and in-Flight Performance in Liquid, Ice and Mixed-Phase Clouds during ARCPAC, Atmospheric Measurement Techniques, 3, 1683–1706, ISSN 1867-1381, https://doi.org/10.5194/amt-3-1683-2010, 2010.

Lawson, P., Gurganus, C., Woods, S., and Bruintjes, R.: Aircraft Observations of Cumulus Microphysics Ranging from the Tropics to Midlatitudes: Implications for a "New" Secondary Ice Process, Journal of the Atmospheric Sciences, 74, 2899 – 2920, https://doi.org/10.1175/JAS-D-17-0033.1, https://journals.ametsoc.org/view/journals/atsc/74/9/jas-d-17-0033.1.xml, 2017.

Lawson, R. P., Stewart, R. E., and Angus, L. J.: Observations and Numerical Simulations of the Origin and Development of Very Large Snowflakes, Journal of the Atmospheric Sciences, 55, 3209–3229, ISSN 0022-4928, 1520-0469, https://doi.org/10.1175/1520-0469(1998)055<3209:OANSOT>2.0.CO;2, 1998.

Lawson, R. P., O'Connor, D., Zmarzly, P., Weaver, K., Baker, B., Mo, Q., and Jonsson, H.: The 2D-S (Stereo) Probe: Design and Preliminary Tests of a New Airborne, High-Speed, High-Resolution Particle Imaging Probe, Journal of Atmospheric and Oceanic Technology, 23, 1462–1477, ISSN 0739-0572, 1520-0426, https://doi.org/10.1175/JTECH1927.1, 2006.

Li, L., Heymsfield, G., Carswell, J., Schaubert, D. H., McLinden, M. L., Creticos, J., Perrine, M., Coon, M., Cervantes, J. I., Vega, M., Guimond, S., Tian, L., and Emory, A.: The NASA High-Altitude Imaging Wind and Rain Airborne Profiler, IEEE Transactions on Geoscience and Remote Sensing, 54, 298–310, ISSN 1558-0644, https://doi.org/10.1109/TGRS.2015.2456501, 2016.

Li, L., Mclinden, M., and Heymsfield, G. M.: High Altitude Imaging Wind and Rain Airborne Profiler (HIWRAP) IMPACTS. Dataset available online from the NASA Global Hydrometeorology Resource Center DAAC, Huntsville, Alabama, U.S.A. , https://doi.org/10.5067/IMPACTS/HIWRAP/DATA101, http://dx.doi.org/10.5067/IMPACTS/HIWRAP/DATA101, 2022.

Lucke, J., Jurkat-Witschas, T., Heller, R., Hahn, V., Hamman, M., Breitfuss, W., Bora, V. R., Moser, M., and Voigt, C.: Icing Wind Tunnel Measurements of Supercooled Large Droplets Using the 12 Mm Total Water Content Cone of the Nevzorov Probe, Atmospheric Measurement Techniques, 15, 7375–7394, ISSN 1867-1381, https://doi.org/10.5194/amt-15-7375-2022, 2022.

Lucke, J., Moser, M., De La Torre Castro, E., Mayer, J., and Voigt, C.: Nevzorov LWC and TWC data from the HALO-AC3 campaign in March and April 2022, https://doi.org/10.1594/PANGAEA.963628, https://doi.org/10.1594/PANGAEA.963628, 2024.

Maahn, M. and Löhnert, U.: Potential of Higher-Order Moments and Slopes of the Radar Doppler Spectrum for Retrieving Microphysical and Kinematic Properties of Arctic Ice Clouds, Journal of Applied Meteorology and Climatology, 56, 263–282, ISSN 1558-8424, 1558-8432, https://doi.org/10.1175/JAMC-D-16-0020.1, 2017.

Maahn, M., Löhnert, U., Kollias, P., Jackson, R. C., and McFarquhar, G. M.: Developing and Evaluating Ice Cloud Parameterizations for Forward Modeling of Radar Moments Using in Situ Aircraft Observations, Journal of Atmospheric and Oceanic Technology, 32, 880–903, ISSN 0739-0572, 1520-0426, https://doi.org/10.1175/JTECH-D-14-00112.1, 2015.

Maherndl, N., Maahn, M., Tridon, F., Leinonen, J., Ori, D., and Kneifel, S.: A Riming-Dependent Parameterization of Scattering by Snowflakes Using the Self-Similar Rayleigh–Gans Approximation, Quarterly Journal of the Royal Meteorological Society, 149, 3562–3581, ISSN 1477-870X, https://doi.org/10.1002/qj.4573, 2023a.

Maherndl, N., Maahn, M., Tridon, F., Leinonen, J., Ori, D., and Kneifel, S.: Data set of simulated rimed aggregates for "A riming-dependent parameterization of scattering by snowflakes using the self-similar Rayleigh-Gans approximation", https://doi.org/10.5281/zenodo.7757034, https://doi.org/10.5281/zenodo.7757034, 2023b.

Maherndl, N., Moser, M., Lucke, J., Mech, M., Risse, N., Schirmacher, I., and Maahn, M.: Quantifying riming from airborne data during the HALO-(AC)[3] campaign, Atmospheric Measurement Techniques, 17, 1475–1495, https://doi.org/10.5194/amt-17-1475-2024, https://amt.copernicus.org/articles/17/1475/2024/, 2024.

Mason, S. L., Chiu, C. J., Hogan, R. J., Moisseev, D., and Kneifel, S.: Retrievals of Riming and Snow Density From Vertically Pointing Doppler Radars, Journal of Geophysical Research: Atmospheres, 123, 13,807–13,834, ISSN 2169-8996, https://doi.org/10.1029/2018JD028603, 2018.

McLinden, M., Li, L., and Heymsfield, G. M.: Cloud Radar System (CRS) IMPACTS. Dataset available online from the NASA Global Hydrometeorology Resource Center DAAC, Huntsville, Alabama, U.S.A. , https://doi.org/10.5067/IMPACTS/CRS/DATA101, http://dx.doi.org/10.5067/IMPACTS/CRS/DATA101, 2022.

McLinden, M. L. W., Li, L., Heymsfield, G. M., Coon, M., and Emory, A.: The NASA GSFC 94-GHz Airborne Solid-State Cloud Radar System (CRS), Journal of Atmospheric and Oceanic Technology, 38, 1001–1017, ISSN 0739-0572, 1520-0426, https://doi.org/10.1175/JTECH-D-20-0127.1, 2021.

McMurdie, L. A., Heymsfield, G., Yorks, J. E., and Braun, S. A.: Investigation of Microphysics and Precipitation for Atlantic Coast-Threatening Snowstorms (IMPACTS) Collection. Data available online [http://ghrc.nsstc.nasa.gov/] from the NASA EOSDIS Global Hydrology Resource Center Distributed Active Archive Center, Huntsville, Alabama, U.S.A , https://doi.org/10.5067/IMPACTS/DATA101, http://dx.doi.org/10.5067/IMPACTS/DATA101, 2019.

McMurdie, L. A., Heymsfield, G. M., Yorks, J. E., Braun, S. A., Skofronick-Jackson, G., Rauber, R. M., Yuter, S., Colle, B., McFarquhar, G. M., Poellot, M., Novak, D. R., Lang, T. J., Kroodsma, R., McLinden, M., Oue, M., Kollias, P., Kumjian, M. R., Greybush, S. J., Heyms-

field, A. J., Finlon, J. A., McDonald, V. L., and Nicholls, S.: Chasing Snowstorms: The Investigation of Microphysics and Precipitation for Atlantic Coast-Threatening Snowstorms (IMPACTS) Campaign, Bulletin of the American Meteorological Society, 103, E1243–E1269, ISSN 0003-0007, 1520-0477, https://doi.org/10.1175/BAMS-D-20-0246.1, 2022.

Mech, M., Kliesch, L.-L., Anhäuser, A., Rose, T., Kollias, P., and Crewell, S.: Microwave Radar/Radiometer for Arctic Clouds (MiRAC): First Insights from the ACLOUD Campaign, Atmospheric Measurement Techniques, 12, 5019–5037, ISSN 1867-1381, https://doi.org/10.5194/amt-12-5019-2019, 2019.

Mech, M., Maahn, M., Kneifel, S., Ori, D., Orlandi, E., Kollias, P., Schemann, V., and Crewell, S.: PAMTRA 1.0: The Passive and Active Microwave Radiative TRAnsfer Tool for Simulating Radiometer and Radar Measurements of the Cloudy Atmosphere, Geoscientific Model Development, 13, 4229–4251, ISSN 1991-959X, https://doi.org/10.5194/gmd-13-4229-2020, 2020.

Mech, M., Ehrlich, A., Herber, A., Lüpkes, C., Wendisch, M., Becker, S., Boose, Y., Chechin, D., Crewell, S., Dupuy, R., Gourbeyre, C., Hartmann, J., Jäkel, E., Jourdan, O., Kliesch, L.-L., Klingebiel, M., Kulla, B. S., Mioche, G., Moser, M., Risse, N., Ruiz-Donoso, E., Schäfer, M., Stapf, J., and Voigt, C.: MOSAiC-ACA and AFLUX - Arctic Airborne Campaigns Characterizing the Exit Area of MOSAiC, Scientific Data, 9, 790, ISSN 2052-4463, https://doi.org/10.1038/s41597-022-01900-7, 2022a.

Mech, M., Risse, N., Marrollo, G., and Paul, D.: ac3airborne, https://doi.org/10.5281/zenodo.7305586, https://doi.org/10.5281/zenodo.7305586, 2022b.

Mech, M., Risse, N., Krobot, P., Paul, D., Schirmacher, I., Schnitt, S., and Crewell, S.: Radar reflectivities at 94 GHz and microwave brightness temperature measurements at 89 GHz during the HALO-AC3 Arctic airborne campaign, https://doi.org/10.1594/PANGAEA.964977, https://doi.org/10.1594/PANGAEA.964977, 2024a.

Mech, M., Risse, N., Ritter, C., Schirmacher, I., and Schween, J. H.: Cloud mask and cloud top altitude from the AMALi airborne lidar on Polar 5 during HALO-AC3 in spring 2022, https://doi.org/10.1594/PANGAEA.964985, https://doi.org/10.1594/PANGAEA.964985, 2024b.

Mitchell, D. L.: Use of Mass- and Area-Dimensional Power Laws for Determining Precipitation Particle Terminal Velocities, Journal of the Atmospheric Sciences, 53, 1710–1723, ISSN 0022-4928, 1520-0469, https://doi.org/10.1175/1520-0469(1996)053<1710:UOMAAD>2.0.CO;2, 1996.

Moisseev, D., von Lerber, A., and Tiira, J.: Quantifying the Effect of Riming on Snowfall Using Ground-Based Observations, Journal of Geophysical Research: Atmospheres, 122, 4019–4037, ISSN 2169-8996, https://doi.org/10.1002/2016JD026272, 2017.

Morrison, H. and Milbrandt, J. A.: Parameterization of Cloud Microphysics Based on the Prediction of Bulk Ice Particle Properties. Part I: Scheme Description and Idealized Tests, Journal of the Atmospheric Sciences, 72, 287–311, ISSN 0022-4928, 1520-0469, https://doi.org/10.1175/JAS-D-14-0065.1, 2015.

Morrison, H., de Boer, G., Feingold, G., Harrington, J., Shupe, M. D., and Sulia, K.: Resilience of Persistent Arctic Mixed-Phase Clouds, Nature Geoscience, 5, 11–17, ISSN 1752-0908, https://doi.org/10.1038/ngeo1332, 2012.

Morrison, H., van Lier-Walqui, M., Fridlind, A. M., Grabowski, W. W., Harrington, J. Y., Hoose, C., Korolev, A., Kumjian, M. R., Milbrandt, J. A., Pawlowska, H., Posselt, D. J., Prat, O. P., Reimel, K. J., Shima, S.-I., van Diedenhoven, B., and Xue, L.: Confronting the Challenge of Modeling Cloud and Precipitation Microphysics, Journal of Advances in Modeling Earth Systems, 12, e2019MS001 689, ISSN 1942-2466, https://doi.org/10.1029/2019MS001689, 2020.

Moser, M., Lucke, J., De La Torre Castro, E., Mayer, J., and Voigt, C.: DLR in situ cloud measurements during HALO-(AC)[3] Arctic airborne campaign, https://doi.org/10.1594/PANGAEA.963247, https://doi.org/10.1594/PANGAEA.963247, 2023.

Moser, M., Voigt, C., Jurkat-Witschas, T., Hahn, V., Mioche, G., Jourdan, O., Dupuy, R., Gourbeyre, C., Schwarzenboeck, A., Lucke, J., Boose, Y., Mech, M., Borrmann, S., Ehrlich, A., Herber, A., Lüpkes, C., and Wendisch, M.: Microphysical and Thermodynamic Phase Analyses of Arctic Low-Level Clouds Measured above the Sea Ice and the Open Ocean in Spring and Summer, Atmospheric Chemistry and Physics, 23, 7257–7280, ISSN 1680-7316, https://doi.org/10.5194/acp-23-7257-2023, 2023.

780 Mróz, K., Battaglia, A., Kneifel, S., von Terzi, L., Karrer, M., and Ori, D.: Linking Rain into Ice Microphysics across the Melting Layer in Stratiform Rain: A Closure Study, Atmospheric Measurement Techniques, 14, 511–529, ISSN 1867-1381, https://doi.org/10.5194/amt-14-511-2021, 2021.

Mülmenstädt, J., Sourdeval, O., Delanoë, J., and Quaas, J.: Frequency of Occurrence of Rain from Liquid-, Mixed-, and Ice-Phase Clouds Derived from A-Train Satellite Retrievals, Geophysical Research Letters, 42, 6502–6509, ISSN 1944-8007, https://doi.org/10.1002/2015GL064604, 2015.

785 Nguyen, C. M., Wolde, M., Battaglia, A., Nichman, L., Bliankinshtein, N., Haimov, S., Bala, K., and Schuettemeyer, D.: Coincident in Situ and Triple-Frequency Radar Airborne Observations in the Arctic, Atmospheric Measurement Techniques, 15, 775–795, ISSN 1867-1381, https://doi.org/10.5194/amt-15-775-2022, 2022.

Ong, C. R., Koike, M., Hashino, T., and Miura, H.: Responses of Simulated Arctic Mixed-Phase Clouds to Parameterized Ice Particle Shape, Journal of the Atmospheric Sciences, 81, 125–152, ISSN 0022-4928, 1520-0469, https://doi.org/10.1175/JAS-D-23-0015.1, 2024.

790 Petters, M. D. and Wright, T. P.: Revisiting Ice Nucleation from Precipitation Samples, Geophysical Research Letters, 42, 8758–8766, ISSN 1944-8007, https://doi.org/10.1002/2015GL065733, 2015.

Rodgers, C. D.: Inverse Methods for Atmospheric Sounding: Theory and Practice, World Scientific, https://doi.org/10.1142/3171, 2000.

Ruiz-Donoso, E., Ehrlich, A., Schäfer, M., Jäkel, E., Schemann, V., Crewell, S., Mech, M., Kulla, B. S., Kliesch, L.-L., Neuber, R., and Wendisch, M.: Small-Scale Structure of Thermodynamic Phase in Arctic Mixed-Phase Clouds Observed by Airborne Remote Sensing during a Cold Air Outbreak and a Warm Air Advection Event, Atmospheric Chemistry and Physics, 20, 5487–5511, ISSN 1680-7316, https://doi.org/10.5194/acp-20-5487-2020, 2020.

Saw, E.-W., Salazar, J. P. L. C., Collins, L. R., and Shaw, R. A.: Spatial Clustering of Polydisperse Inertial Particles in Turbulence: I. Comparing Simulation with Theory, New Journal of Physics, 14, 105 030, ISSN 1367-2630, https://doi.org/10.1088/1367-2630/14/10/105030, 2012a.

800 Saw, E.-W., Shaw, R. A., Salazar, J. P. L. C., and Collins, L. R.: Spatial Clustering of Polydisperse Inertial Particles in Turbulence: II. Comparing Simulation with Experiment, New Journal of Physics, 14, 105 031, ISSN 1367-2630, https://doi.org/10.1088/1367-2630/14/10/105031, 2012b.

Schirmacher, I., Kollias, P., Lamer, K., Mech, M., Pfitzenmaier, L., Wendisch, M., and Crewell, S.: Assessing Arctic Low-Level Clouds and Precipitation from above – a Radar Perspective, Atmospheric Measurement Techniques, 16, 4081–4100, ISSN 1867-1381, https://doi.org/10.5194/amt-16-4081-2023, 2023.

805 Schirmacher, et al.: Clouds and precipitation in the initial phase of marine cold air outbreaks as observed by airborne remote sensing [in prep.], 2024.

Seifert, A., Leinonen, J., Siewert, C., and Kneifel, S.: The Geometry of Rimed Aggregate Snowflakes: A Modeling Study, Journal of Advances in Modeling Earth Systems, 11, 712–731, ISSN 1942-2466, https://doi.org/10.1029/2018MS001519, 2019.

810 Shaw, R. A., Kostinski, A. B., and Larsen, M. L.: Towards Quantifying Droplet Clustering in Clouds, Quarterly Journal of the Royal Meteorological Society, 128, 1043–1057, ISSN 1477-870X, https://doi.org/10.1256/003590002320373193, 2002.

Shupe, M. D. and Intrieri, J. M.: Cloud Radiative Forcing of the Arctic Surface: The Influence of Cloud Properties, Surface Albedo, and Solar Zenith Angle, Journal of Climate, 17, 616–628, ISSN 0894-8755, 1520-0442, https://doi.org/10.1175/1520-0442(2004)017<0616:CRFOTA>2.0.CO;2, 2004.

Sorooshian, A., Alexandrov, M. D., Bell, A. D., Bennett, R., Betito, G., Burton, S. P., Buzanowicz, M. E., Cairns, B., Chemyakin, E. V., Chen, G., Choi, Y., Collister, B. L., Cook, A. L., Corral, A. F., Crosbie, E. C., van Diedenhoven, B., DiGangi, J. P., Diskin, G. S., Dmitrovic, S., Edwards, E.-L., Fenn, M. A., Ferrare, R. A., van Gilst, D., Hair, J. W., Harper, D. B., Hilario, M. R. A., Hostetler, C. A., Jester, N., Jones, M., Kirschler, S., Kleb, M. M., Kusterer, J. M., Leavor, S., Lee, J. W., Liu, H., McCauley, K., Moore, R. H., Nied, J., Notari, A., Nowak, J. B., Painemal, D., Phillips, K. E., Robinson, C. E., Scarino, A. J., Schlosser, J. S., Seaman, S. T., Seethala, C., Shingler, T. J., Shook, M. A., Sinclair, K. A., Smith Jr., W. L., Spangenberg, D. A., Stamnes, S. A., Thornhill, K. L., Voigt, C., Vömel, H., Wasilewski, A. P., Wang, H., Winstead, E. L., Zeider, K., Zeng, X., Zhang, B., Ziemba, L. D., and Zuidema, P.: Spatially Coordinated Airborne Data and Complementary Products for Aerosol, Gas, Cloud, and Meteorological Studies: The NASA ACTIVATE Dataset, Earth System Science Data, 15, 3419–3472, ISSN 1866-3508, https://doi.org/10.5194/essd-15-3419-2023, 2023.

Stachlewska, I. S., Neuber, R., Lampert, A., Ritter, C., and Wehrle, G.: AMALi – the Airborne Mobile Aerosol Lidar for Arctic Research, Atmospheric Chemistry and Physics, 10, 2947–2963, ISSN 1680-7316, https://doi.org/10.5194/acp-10-2947-2010, 2010.

Sun, Z. and Shine, K. P.: Studies of the Radiative Properties of Ice and Mixed-Phase Clouds, Quarterly Journal of the Royal Meteorological Society, 120, 111–137, ISSN 1477-870X, https://doi.org/10.1002/qj.49712051508, 1994.

Toohey, D., Noone, D., and Wein, E.: Water Isotope System for Precipitation and Entrainment Research (WISPER) IMPACTS. Dataset available online from the NASA Global Hydrometeorology Resource Center DAAC, Huntsville, Alabama, U.S.A. , https://doi.org/10.5067/IMPACTS/WISPER/DATA101, http://dx.doi.org/10.5067/IMPACTS/WISPER/DATA101, 2022.

Tridon, F., Battaglia, A., Chase, R. J., Turk, F. J., Leinonen, J., Kneifel, S., Mroz, K., Finlon, J., Bansemer, A., Tanelli, S., Heymsfield, A. J., and Nesbitt, S. W.: The Microphysics of Stratiform Precipitation During OLYMPEX: Compatibility Between Triple-Frequency Radar and Airborne In Situ Observations, Journal of Geophysical Research: Atmospheres, 124, 8764–8792, ISSN 2169-8996, https://doi.org/10.1029/2018JD029858, 2019.

Tridon, F., Silber, I., Battaglia, A., Kneifel, S., Fridlind, A., Kalogeras, P., and Dhillon, R.: Highly Supercooled Riming and Unusual Triple-Frequency Radar Signatures over Antarctica, Atmospheric Chemistry and Physics Discussions, pp. 1–34, ISSN 1680-7316, https://doi.org/10.5194/acp-2022-136, 2022.

Turner, D. D.: Arctic Mixed-Phase Cloud Properties from AERI Lidar Observations: Algorithm and Results from SHEBA, Journal of Applied Meteorology and Climatology, 44, 427–444, ISSN 1520-0450, 0894-8763, https://doi.org/10.1175/JAM2208.1, 2005.

Waitz, F., Schnaiter, M., Leisner, T., and Järvinen, E.: In Situ Observation of Riming in Mixed-Phase Clouds Using the PHIPS Probe, Atmospheric Chemistry and Physics, 22, 7087–7103, ISSN 1680-7316, https://doi.org/10.5194/acp-22-7087-2022, 2022.

Walbröl, A., Michaelis, J., Becker, S., Dorff, H., Ebell, K., Gorodetskaya, I., Heinold, B., Kirbus, B., Lauer, M., Maherndl, N., Maturilli, M., Mayer, J., Müller, H., Neggers, R. A. J., Paulus, F. M., Röttenbacher, J., Rückert, J. E., Schirmacher, I., Slättberg, N., Ehrlich, A., Wendisch, M., and Crewell, S.: Contrasting extremely warm and long-lasting cold air anomalies in the North Atlantic sector of the Arctic during the HALO-$(\mathcal{AC})^3$ campaign, Atmospheric Chemistry and Physics, 24, 8007–8029, https://doi.org/10.5194/acp-24-8007-2024, https://acp.copernicus.org/articles/24/8007/2024/, 2024.

Wendisch, M., Crewell, S., Ehrlich, A., Herber, A., Kirbus, B., Lüpkes, C., Mech, M., Abel, S. J., Akansu, E. F., Ament, F., Aubry, C., Becker, S., Borrmann, S., Bozem, H., Brückner, M., Clemen, H.-C., Dahlke, S., Dekoutsidis, G., Delanoë, J., De La Torre Castro, E., Dorff, H., Dupuy, R., Eppers, O., Ewald, F., George, G., Gorodetskaya, I. V., Grawe, S., Groß, S., Hartmann, J., Henning, S., Hirsch, L., Jäkel, E.,

38

Joppe, P., Jourdan, O., Jurányi, Z., Karalis, M., Kellermann, M., Klingebiel, M., Lonardi, M., Lucke, J., Luebke, A., Maahn, M., Maherndl, N., Maturilli, M., Mayer, B., Mayer, J., Mertes, S., Michaelis, J., Michalkov, M., Mioche, G., Moser, M., Müller, H., Neggers, R., Ori, D., Paul, D., Paulus, F., Pilz, C., Pithan, F., Pöhlker, M., Pörtge, V., Ringel, M., Risse, N., Roberts, G. C., Rosenburg, S., Röttenbacher, J., Rückert, J., Schäfer, M., Schäfer, J., Schemannn, V., Schirmacher, I., Schmidt, J., Schmidt, S., Schneider, J., Schnitt, S., Schwarz, A., Siebert, H., Sodemann, H., Sperzel, T., Spreen, G., Stevens, B., Stratmann, F., Svensson, G., Tatzelt, C., Tuch, T., Vihma, T., Voigt, C., Volkmer, L., Walbröl, A., Weber, A., Wehner, B., Wetzel, B., Wirth, M., and Zinner, T.: Overview: Quasi-Lagrangian observations of Arctic air mass transformations – Introduction and initial results of the HALO–(AC)^3 aircraft campaign, EGUsphere, 2024, 1–46, https://doi.org/10.5194/egusphere-2024-783, https://egusphere.copernicus.org/preprints/2024/egusphere-2024-783/, 2024.

Wood, A. M., Hwang, W., and Eaton, J. K.: Preferential Concentration of Particles in Homogeneous and Isotropic Turbulence, International Journal of Multiphase Flow, 31, 1220–1230, ISSN 0301-9322, https://doi.org/10.1016/j.ijmultiphaseflow.2005.07.001, 2005.